

Evaluation of laser heterodyne radiometry for numerical weather prediction applications

Fiona Smith¹  | Stephan Havemann¹  | Alex Hoffmann²  | William Bell^{1,†} |
Damien Weidmann²  | Stuart Newman¹

¹Met Office, Exeter, UK

²Space Science and Technology Department, STFC Rutherford Appleton Laboratory, Oxfordshire, UK

Correspondence

Damien Weidmann, Space Science & Technology Department, STFC Rutherford Appleton Laboratory, Harwell Campus, Didcot, OX11 0QX, UK.

Email: damien.weidmann@stfc.ac.uk

Fiona Smith, Met Office, FitzRoy Road, Exeter, Devon, EX1 3PB, UK.

Email: fiona.smith@metoffice.gov.uk

[†]Present address European Centre for Medium-Range Weather Forecasts, Shinfield Park, Reading, RG2 9AX, UK.

Funding information

Science and Technology Facilities Council, ST/M007154/1.

This article reports the results of a preliminary mission study to assess the potential of space-borne laser heterodyne radiometry (LHR) for the remote sensing of temperature for assimilation in a numerical weather prediction (NWP) model. The LHR instruments are low cost and small in size, lending themselves to a wide variety of satellite platforms. The impact of different configurations of an idealized LHR instrument is assessed against the Infrared Atmospheric Sounding Interferometer (IASI), via single-column linear information content analysis, using inputs consistent with the background errors of the Met Office 4D-Var assimilation system. Multiplexed configurations give promising results, in particular for sounding of upper-atmospheric temperatures.

KEYWORDS

DFS, IASI, information content, laser heterodyne radiometer, numerical weather prediction, temperature sounding, upper atmosphere

1 | INTRODUCTION

Steady progress has been made over the last two decades in improving the skill of global numerical weather prediction (NWP) models, which now provide the basis for forecast guidance 7 days ahead. Much of the gain in skill is attributable to the improved use of satellite data, through improved data assimilation systems, as well as through the growth of a comprehensive and diverse satellite observing system (e.g. Collard *et al.*, 2011, and references therein).

Operational NWP centres typically assess the contribution to forecast skill from each existing component of the observing system using both observing system experiments (OSEs), in which specific types of data are denied from the forecast system, and adjoint techniques such as forecast sensitivity to observation impact (FSOI: e.g. Lorenc and Marriott, 2014). These paint a broadly consistent picture, showing that the radiometric measurements from hyperspectral infrared sounding instruments, together with the microwave instruments, provide most benefit for NWP.

One of the hyperspectral sounders used in NWP is the Infrared Atmospheric Sounding Interferometer (IASI: Siméoni *et al.*, 1997). The instrument measures a spectral range that spans the thermal infrared (IR) ($645\text{--}2,760\text{ cm}^{-1}$) at a moderately high spectral resolution of 0.5 cm^{-1} and with relatively good radiometric sensitivity (noise equivalent delta temperature NEdT of $0.15\text{--}0.2\text{ K}$ across the long-wave temperature sounding channels). IASI's good radiometric performance is coupled with excellent reliability and data availability, and the instrument represents current state-of-the-art in hyperspectral IR sounding. IASI's major contribution to the observing network comes at the cost of size, weight and power (1.4 m^3 , 210 kg and 200 W), which means it must be deployed on dedicated and costly satellite platforms.

For meteorological sounding applications targeting temperature and humidity, most useful information is confined to relatively small sub-regions of the thermal infrared, specifically the regions around the $\text{CO}_2\text{ } \nu_2$ band centred at 667 cm^{-1} for temperature sounding, and the $\text{H}_2\text{O } \nu_2$ band centred at

This is an open access article under the terms of the Creative Commons Attribution License, which permits use, distribution and reproduction in any medium, provided the original work is properly cited.

© 2018 The Authors. *Quarterly Journal of the Royal Meteorological Society* published by John Wiley & Sons Ltd on behalf of the Royal Meteorological Society.

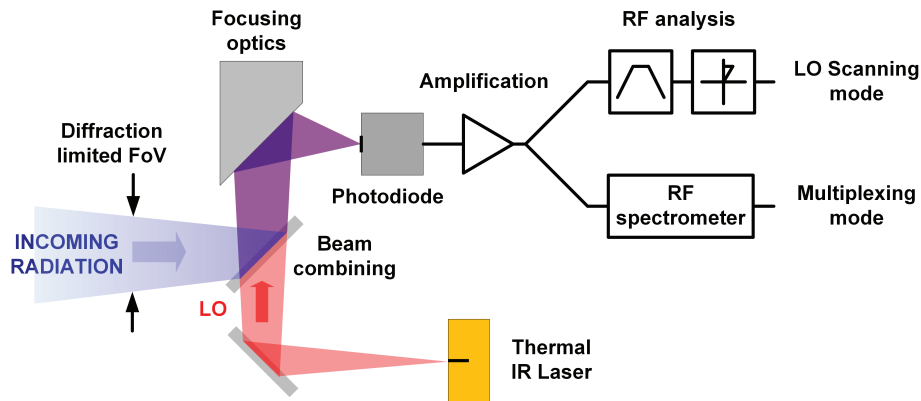


FIGURE 1 Schematic diagram of a laser heterodyne radiometer [Colour figure can be viewed at wileyonlinelibrary.com]

$1,595\text{ cm}^{-1}$ for humidity sounding. This raises the general question as to whether more compact spectro-radiometers could be developed, covering only these key spectral regions to provide equivalent, or better, performance for meteorological applications at lower cost.

Infrared heterodyne spectro-radiometers (LHRs) based on carbon dioxide lasers and tuneable lead-salt diode lasers have been used in atmospheric research for decades (Allario *et al.*, 1983). However, their features (size, the requirement for cryogenic operation, and power requirements) preclude them for deployment on small satellites. The development of quantum cascade lasers (QCLs) during the 1990s heralded the advent of solid state, compact, robust and continuously tuneable mid-IR laser sources, well suited to providing thermal infrared local oscillators. Since then, the technology has matured considerably such that QCLs can be considered for operational deployment in space (Myers *et al.*, 2015).

QCL-based LHR technology has advanced rapidly in the last decade, initially for trace-gas detection in Earth observation and planetary applications (Weidmann *et al.*, 2007a). Atmospheric science applications have included ozone profiling (Weidmann *et al.*, 2007b), multi-constituent profiling (Weidmann *et al.*, 2011a; Tsai *et al.*, 2012), and most recently atmospheric CO_2 measurements (Hoffmann *et al.*, 2016). Developments are currently underway to miniaturize the LHRs using optical integration technologies (Weidmann *et al.*, 2011b) and make them suitable for small satellite applications (Weidmann *et al.*, 2017). As well as the compact size, QCL LHRs offer the combined advantages of ultra-high spectral resolution ($\sim 0.001\text{ cm}^{-1}$) over narrow spectral microwindows ($0.1\text{--}1\text{ cm}^{-1}$); high horizontal resolution due to the inherently narrow field-of-view (a few hundred metres or less from low Earth orbit); and ideally a radiometric sensitivity determined by the shot-noise induced by the random arrival of photons onto the detectors.

The next generation of European operational meteorological satellites are due to launch in the next few years, and will serve weather and climate applications until 2040. There is therefore a window of opportunity to evaluate and demonstrate new technologies in time to be considered as components of future operational missions. The purpose of

this preliminary study was to establish the potential for a nadir-viewing LHR to meet future NWP requirements, primarily by assessing the expected performance of an LHR in profiling temperature from low Earth orbit (LEO) and geostationary orbit (GEO) platforms, using an information content method. IASI has been used as a benchmark so that the potential of an LHR can be placed in the context of a well-known, high quality, operational spectrometer.

The principles of laser heterodyne radiometry are briefly introduced in section 2. Section 3 describes the main orbit configurations considered in this study and the attendant constraints on integration and sampling times. In section 4, the framework for the assessment of the idealised LHR performance is described, including the Degrees of Freedom for Signal (DFS) metric. Section 5 details the inputs to the DFS calculations including background and instrument error models, input profiles, and the radiative transfer modelling details. The main results of the study are given in sections 6–8. Some future directions are outlined in section 9, and conclusions are drawn in section 10.

2 | A BRIEF INTRODUCTION TO LASER HETERODYNE RADIOMETRY

Laser heterodyne radiometers (LHRs) bear some similarities to radio receivers, but transposed into the optical domain. They are passive sounders that use a laser source, in this case a QCL, as a local oscillator (LO). Figure 1 shows a simplified schematic of an LHR, illustrating its operating principles. The thermal IR radiation to be analysed is collected by the primary mirror (not shown). It is then superimposed with the coherent optical field of the LO. The requirement to match the wave-fronts of the two fields determines the maximum tolerable angular misalignment of the LO and source beams, which in turn determines the field-of-view of the instrument. The two superimposed fields are imaged onto a high-speed photodiode serving as a photomixer, which down-converts the spectral information of the incoming radiation centred at the LO frequency and within the electrical bandwidth of the photomixer to the radio-frequency

(RF) domain. This signal is usually called the intermediate frequency (IF).

2.1 | Modes of operation

The LHR makes measurements at very high spectral resolution across a small region of the spectrum referred to here as a microwindow. The instrument can be operated in one of two modes, depending on whether the LO frequency is fixed or continuously tuned.

In Multiplexing Mode, the LO frequency is fixed and the spectral coverage of the instrument is defined by the photodiode electrical bandwidth. RF spectral analysis is required to reconstruct a spectrum, for example using a bank of IF filters (Mumma *et al.*, 1982), an acousto-optical spectrometer (Schieder *et al.*, 1989) or correlation spectrometers. This technology sets the spectral resolution. It is currently feasible and conservative to assume up to 20 channels, each as narrow as 0.005 cm^{-1} , covering a microwindow of 0.1 cm^{-1} . Currently available resonant optical cavity mercury cadmium telluride photodiodes achieve 0.1 cm^{-1} (3 GHz) bandwidth. In the near future, quantum-well-based structures are very promising, as 3.5 cm^{-1} (>100 GHz) bandwidth has been demonstrated (Grant *et al.*, 2006). An Advanced Multiplexing Mode is defined as relying on such devices, which would allow a 1 cm^{-1} bandwidth. Multiplexing Mode is efficient in terms of integration time, but adds to the instrument complexity.

On the other hand, in Scanning Mode, the spectral resolution is set by the bandwidth of a fixed RF filter, but the spectral coverage is obtained by continuously tuning the LO over a given frequency range, usually limited by the laser source. This is easier to implement technically, but the sequential acquisition has the drawback that the total time needed to measure across the microwindow is much longer than for Multiplexing Mode. For the purposes of this study, a 0.1 cm^{-1} microwindow is considered, at a maximum spectral resolution of 0.001 cm^{-1} .

2.2 | Instrument trade-offs

Since the throughput (also known as etendue or $A\Omega$ product) is constant in an LHR relying on a single detector (Siegman, 1966), only the spectral resolution and the integration time, τ (i.e. the time to acquire a single spectral channel), determine the instrument noise, governed by relationships that will be described in section 5.3.1. The total acquisition time, t , represents the time required to acquire a full spectrum for a single field of view (FOV). Thus, in an ideal situation, the acquisition time in Scanning mode is simply $t = \tau \times n$, where n is the number of channels in a microwindow. In Multiplexing mode, where channels are measured simultaneously, we assume $t = \tau$. Here, a single detector instrument (one single FOV) is assumed, but cross-track scanning could be implemented using scanning mirrors to control the FOV, if the acquisition time was sufficient.

TABLE 1 LHR modes of operation considered in this study. SSM, MM and AMM stand for Spectral Scanning mode, Multiplexing mode and Advanced Multiplexing mode respectively

Mode	Spectral resolution (cm^{-1})	Microwindow width (cm^{-1})	Sub-sampling resolution (cm^{-1})	Number of channels
SSM	0.001	0.1	-	100
SSM	0.001	0.1	0.002	50
SSM	0.001	0.1	0.004	25
SSM	0.001	0.1	0.006	17
SSM	0.001	0.1	0.008	13
SSM	0.002	0.1	-	50
SSM	0.002	0.1	0.004	25
SSM	0.002	0.1	0.006	17
SSM	0.002	0.1	0.008	13
MM	0.005	0.1	-	20
MM	0.01	0.1	-	10
AMM	0.005	1.0	-	200
AMM	0.01	1.0	-	100
AMM	0.02	1.0	-	50

There is thus a trade-off to be made between the spectral resolution and the microwindow size for a given acquisition time: a wider microwindow and higher spectral resolution will both result in more channels, reducing integration time in Scanning mode. Higher spectral resolution comes at the expense of a lower signal-to-noise ratio (SNR), but may allow higher vertical resolution in the sounding, whereas a wider microwindow gives an increase in the number of spectral lines available for sounding.

The integration time is probably the most important constraint on the feasibility of a space-borne LHR instrument for NWP, as the acquisition time will be highly constrained by the satellite orbit parameters for low earth (LEO), and revisit time for geostationary orbit (GEO). It can therefore be anticipated that spectral multiplexing will give better SNR performance.

The LHR spectral acquisition modes that were considered in this study have been summarized in Table 1. Within each mode, various sub-modes are possible, such as:

- acquiring non-contiguous samples, such that spectral resolution is higher than sampling resolution. This will only be of potential benefit in Spectral Scanning mode, as the main effect would be to allow an increase in integration time within the same acquisition time.
- trading off the spectral resolution and SNR (see section 5.3.1). For example, in Multiplexing mode, rather than using 20 channels of 0.005 cm^{-1} resolution, 10 channels of 0.01 cm^{-1} could be considered.

One further possibility is to put two or more different LHR instrument modules (or laser sub-systems) together on the same platform, to extend spectral coverage and diversity. The number of permutations to optimize information retrieval for multiple LHRs is very large, and will not be considered

further in this study. However, it could be an attractive option for a combined temperature and water vapour (or ozone) sounding mission.

3 | SATELLITE PLATFORM AND VIEWING MODE

This study focuses on the application of a nadir-viewing, satellite-mounted LHR for temperature sounding, in either LEO or GEO. The LHR is also appropriate for a limb-sounding mission in passive or solar occultation mode on LEO satellites, for example as a stratospheric temperature-sounding mission, but investigating this viewing mode is beyond the scope of this study.

3.1 | LEO satellite

A typical satellite in sun-synchronous LEO at an altitude of 700–800 km has a tangential speed of ~ 7.5 km/s. An observation's acquisition time is therefore strongly limited if one wishes to maintain spatial resolution, and homogeneity of the scene observed. A comparison with existing high-resolution thermal infrared instruments gives some indication of the potential acquisition times to be considered. For instance:

- IASI, a cross-track scanner, with 30 fields of regard (FOR) plus calibration targets within a 15 s scan cycle, has an interferogram acquisition time of 0.15 s per FOR (four FOVs within each FOR are acquired simultaneously);
- TES (Tropospheric Emission Spectrometer) has several modes of operation, including limb sounding and nadir viewing. For the “Step&Stare” nadir-viewing mode, the acquisition time is 4 s, giving one footprint approximately every 45 km along the satellite track. In this time, the satellite itself moves 39 km.

Motion compensation can be achieved at instrument level using a scan mirror. IASI uses a two-axis scan mirror to achieve motion compensation while cross-track scanning. Without cross-track scanning (requiring only a one-axis scan mirror), a maximum acquisition time of 1–2 s would allow relatively dense sampling along track whilst keeping scene heterogeneity low.

At the longest acquisition times, even though motion compensation can maintain the ground point, the observation will encompass a wide swath of upper atmosphere (given the small ground footprint of the LHR, the sampled footprint will be a very narrow wedge). This will introduce some heterogeneity into the measured scene. For a mode like the TES “Step&Stare” mode, with 4 s acquisition time, the sampled region expands from the nominal nadir footprint to ~ 0.5 km at 10 km altitude, and ~ 2.8 km at 50 km altitude. However, heterogeneity in the upper levels is unlikely to pose too much of a problem, as the length-scales on which temperature varies are greater in the upper atmosphere. Water vapour content, which

is spatially highly variable in the troposphere, is extremely low in the stratosphere.

3.2 | GEO satellite

With GEO platforms, the satellite orbits at a velocity that maintains a fixed position relative to the Earth, which means that the acquisition time can be longer per dwell. The constraints are the changing of the measurement scene during the acquisition (for example, features such as clouds drifting in and out of the field of view), and the requirement to cover the desired portions of the Earth disc at reasonable repeat times. Five seconds was chosen as an acceptable maximum acquisition time from a GEO platform.

3.3 | Choice of acquisition time

As a result of the previous considerations, three acquisition times have been considered in this study:

- $t = 0.15$ s, representing a cross-track scanning mode, and equivalent to the acquisition time for IASI,
- $t = 1$ s, representing a push-broom measurement mode for an LEO instrument,
- $t = 5$ s, representing measurement time for a GEO instrument or an LEO instrument in point-and-stare mode.

The impact of these different acquisition times on the performance of the LHR is taken into account via the instrument noise model described in section 5.3.1. Note that because of the small size of the LHR, even without implementing a scan mirror, several instruments could be mounted on the satellite platform with different viewing angles so that in push-broom or point-and-stare modes, a swath could be measured.

4 | METHOD FOR ASSESSING THE SUITABILITY OF LHR FOR NWP

The potential of the LHR was assessed via information content calculations for a profile retrieval of temperature with input assumptions appropriate for NWP applications. The chosen measure of information content used in this study is degrees of freedom for signal (DFS), derived from linear optimal estimation (OE: e.g. Rodgers, 2000). DFS is chosen because it is a widely used and well-understood measure that imparts information on how much the error in a retrieval has been reduced overall from that of the prior state by the incorporation of information from an observation. The approach taken in this study is therefore consistent with OE information content studies for atmospheric chemistry (e.g. Tsai *et al.*, 2012, for the LHR).

Most NWP models assimilate data via variational analysis (usually three-dimensional (3D-) or 4D-Var: e.g. Rawlins *et al.*, 2007). The 1D OE system used here is a huge simplification of the actual NWP 4D-Var analysis system. However,

TABLE 2 Summary of instrument parameters for a compact and ruggedized infrared LHR compared with those of IASI

Parameter	IASI	LHR	Comment
Size Weight Power	1.452 m ³ 210 kg 200 W	0.016 m ³ 3.9 kg 25 W	SSP or piggybacking LHRs offer the possibility of (a) cost reductions compared to larger instruments, and (b) multiple instruments (on a constellation) giving improved spatial and temporal coverage within a single large satellite instrument budget.
Spectral resolution	0.35–0.5 cm ⁻¹	~0.001 cm ⁻¹	The LHR's spectral resolution enables (a) derivation of altitude information from measured line shapes, and (b) improved spectral selectivity.
Radiometric sensitivity	0.25 K	0.05–5.0 K	Radiometric sensitivity is a key parameter in determining the impact of a radiance observation in an NWP system. For the LHR this will be strongly dependent on integration time and resolution. The trade-off is part of this study.
Nadir footprint	12 km	~50–70 m (from LEO)	The LHR's inherently small FOV could allow (a) increased observation frequency by making better use of clear sky between clouds, and (b) intelligent targeting of "interesting" weather at high spatial resolution (particularly from GEO).
Spectral coverage	645–2,762 cm ⁻¹ (15.5–3.62 μm)	Up to a maximum of 15 cm ⁻¹ (here, <1 cm ⁻¹)	For NWP, well-defined and narrow measurement channels should provide sufficient information. These are accessible with conventional QCL devices targeted at specific wavelengths.

a 1D analogue is a useful tool to establish preliminary performance data, especially for an inherently vertical problem such as satellite sounding. By comparing the results for a new instrument with an instrument already in operational use (in this case the LHR and IASI respectively), we can use the DFS measure to give an indication of whether the new instrument will provide benefit in a 4D-Var assimilation system. The theory is covered in section 4.1 and the use of IASI as a benchmark in section 4.2. The inputs to the DFS calculations are detailed in section 5.

4.1 | Theoretical background to the information content study

DFS is calculated according to the equation:

$$DFS = \text{Tr}(\mathbf{I} - \mathbf{A}\mathbf{B}^{-1}) \quad (1)$$

where \mathbf{A} is the analysis (or retrieval) error covariance matrix and \mathbf{B} is the background (or *a priori*) error covariance matrix. According to optimal estimation theory, \mathbf{A} can be calculated as:

$$\mathbf{A} = (\mathbf{B}^{-1} + \mathbf{H}^T\mathbf{R}^{-1}\mathbf{H})^{-1}, \quad (2)$$

where \mathbf{R} is the combined instrument and representation error covariance matrix (including forward model error, as defined in Janjić *et al.*, 2017) and \mathbf{H} is the Jacobian matrix. The Jacobian matrix represents the change in radiance of each channel resulting from a unit change in each element of the input atmospheric state vector. A radiative transfer model is required to simulate \mathbf{H} ; the Havemann Taylor Fast Radiative Transfer Model (HT-FRTC; Havemann, 2006; Havemann *et al.*, 2016) was chosen for this study.

DFS is a scalar measure: it is effectively an average of the impact of the observation over the whole of the state vector relative to the information contained in the background profile. It is usually interpreted to show the number of independent pieces of information imparted by the observation to

the retrieval, but gives no indication of where this new information is located in profile space. In order to examine which parts of the atmospheric column the LHR instrument impacts, it is necessary to examine the averaging kernels, \mathbf{KH} , where \mathbf{K} is the optimal estimation weight matrix, also known as the Kalman Gain matrix. Averaging kernels are the functions that spread the information from the observation onto the retrieval/analysis grid. They are calculated using the equation

$$\mathbf{KH} = (\mathbf{B}^{-1} + \mathbf{H}^T\mathbf{R}^{-1}\mathbf{H})^{-1}\mathbf{H}^T\mathbf{R}^{-1}\mathbf{H}. \quad (3)$$

4.2 | Comparing the LHR with IASI

The performance of the LHR was assessed by comparison with IASI. Table 2 summarises the characteristics of a QCL-based LHR in comparison with IASI. IASI, as a cross-track scanner, has a wide swath of 2,200 km and a relatively large footprint size of 12.5 km, and as such delivers good spatial coverage. A LEO LHR, on the other hand, will have poor noise performance as a cross-track scanner because of the short integration time (see sections 7.4 and 7.5). A single-view instrument would have limited impact on NWP, where the main advantage of satellite data is in the wide global coverage that sounders typically provide. However, a swath can be created by mounting instruments side-by-side, but we envisage a narrower and/or more widely spaced swath than for IASI.

On the other hand, the FOV for the LHR will be very small, typically of the order of 0.1 mrad, yielding ground footprints of approximately 70 m from LEO, or 3–4 km from GEO. This offers an advantage in terms of improved scene homogeneity, provided the acquisition time is suitably short. It is worth noting that an IR instrument with a small FOV is of interest to the NWP community. The proposal to reduce the field-of-view size of the NOAA-series hyperspectral sounder (Wang *et al.*, 2016) has support from operational NWP centres, despite the

implication that the instrument noise would increase, because the radiative transfer modelling of cloudy scenes is generally better from more homogeneous fields of view.

The assessment of differences in viewing geometry between the LHR and IASI is difficult and is not considered in quantitative detail here. However, if an LHR could potentially deliver benefits comparable to IASI for a given FOV, but at relatively low cost, it would be worth further study. An advantage of the small size and low cost is that it is an ideal candidate for mounting on a constellation of satellites, increasing the options for improving spatial and temporal coverage.

5 | INPUTS TO THE INFORMATION CONTENT CALCULATIONS

This section describes the inputs used to calculate the DFS and averaging kernels, according to the equations in section 4.1.

5.1 | Radiative transfer model

As described above, the RT model used in this study is the HT-FRTC, run in “line-by-line” mode. The LHR instrument line-shape function (ILS) was approximated by a top-hat function whose width was set to the instrument spectral resolution (consistent with the use of a low-pass RF filter). Radiative transfer simulations were run at 0.0001 cm^{-1} resolution and subsequently integrated over the ILS. For IASI, the standard Gaussian-apodised Level 1c channel definitions were used.

5.2 | Background error covariance matrix

The DFS, and the form of the averaging kernels, are strongly dependent on the background error covariance matrix, \mathbf{B} . The same instrument will have a higher information content in different retrieval systems, especially where a climatological \mathbf{B} is used (Hilton *et al.*, 2009a). For standalone retrieval schemes, \mathbf{B} is usually estimated from climatological variability and it is not uncommon to design the form of \mathbf{B} such that the retrieval would have certain desired properties (see for example Deeter *et al.* (2010), where a justification for changes in the *a priori* covariance matrix in a retrieval system is made). The main difference in approach between an NWP-based information content study and a traditional OE retrieval for chemistry and air-quality applications is that NWP benefits from a more accurate background (or prior) state estimate, obtained by projecting a previous analysis forward in time (by 6–12 h) using a forecast model. The background error covariance matrix is an inherent part of the system, being derived from the model itself. The results in this study would vary if a different NWP model were assumed; nevertheless, the results

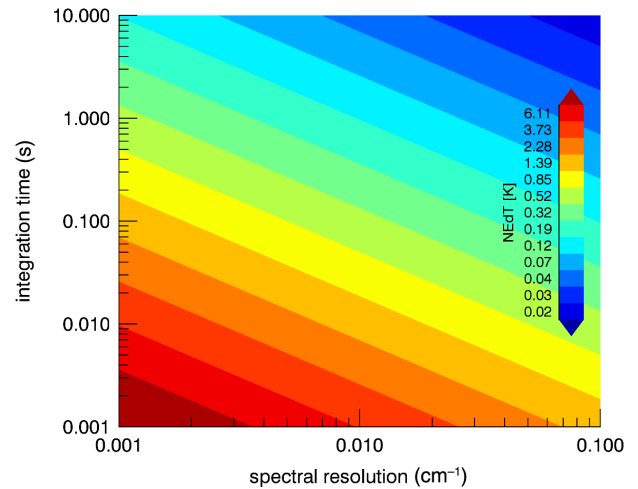


FIGURE 2 LHR noise equivalent delta temperature at the ideal shot-noise limit, as a function of receiver (filter) double-side bandwidth (here given in equivalent spectral resolution) and integration time. The instrument is measuring around 750 cm^{-1} , with a heterodyne efficiency of 0.5, has an optical efficiency of 1, and looks at a blackbody of 280 K reference temperature [Colour figure can be viewed at wileyonlinelibrary.com].

obtained here are broadly representative of the expected effect of LHR data on current NWP models.

The \mathbf{B} matrix used in this study was a 1D representation of the temperature-based component of the 4D-Var error covariance in operational use at the Met Office in March 2012. It was constructed using a randomisation method (Wlasak, 2013; similar to the technique used by Andersson *et al.*, 2000). In 4D-Var, the errors in the control vector are assumed to follow a Gaussian distribution of zero mean and unit variance. Various transform functions are used to map the elements of the control vector to physical variables (Wlasak and Cullen, 2014). The randomisation method makes a large number of vertical samples of the control vector error using locations across the globe. These error vectors are mapped back into model variables (such as temperature) through the 4D-Var parameter transforms. The average of the outer products of these individual error vectors gives the 1D \mathbf{B} matrix. The matrix employed here was described in detail and used extensively in Smith (2015) and in Eyre and Hilton (2013) for information content studies. The standard deviation of the errors in profile space can be seen in the black lines of Figure 5 (see figure 3.3c of Smith (2015) for the covariance structure).

5.3 | Observation error covariance matrix

5.3.1 | LHR noise model

The LHR instrument noise model is based on an ideal receiver significantly dominated by shot noise (Figure 2). In this case, the noise equivalent power (NEP) of the LHR is expressed, following Weidmann *et al.* (2007a), as

$$NEP = \rho \frac{h\nu}{\eta} \sqrt{\frac{B}{\tau}}, \quad (4)$$

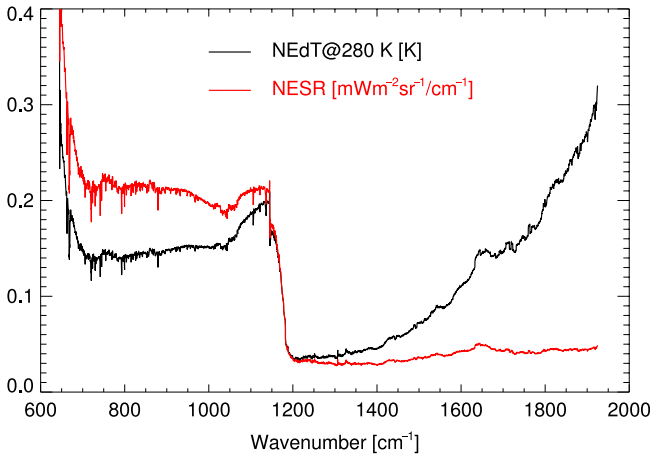


FIGURE 3 IASI noise equivalent delta temperature, at a reference temperature of 280 K, and noise equivalent spectral radiance as used in this study to calculate DFS [Colour figure can be viewed at wileyonlinelibrary.com]

where h is the Planck constant, ν is the optical frequency, η is the detector heterodyne efficiency, B the receiver bandwidth (or spectral resolution) and τ the integration time. The optional unitless degradation factor ρ can be used as a multiplier to account for noise larger than the ideal shot-noise limit; in ground-based solar occultation experimental studies, this has been found to be of the order of 2–5 (Hoffmann *et al.*, 2016). This noise model is used to define the diagonal elements of the \mathbf{R} matrix. Measurements on the ground-based LHR demonstrator have shown that the measurement noise covariance matrix is diagonal.

The throughput (G) of a heterodyne receiver corresponds to that of a diffraction-limited laser beam and can thus be written as the square of the operating wavelength (λ), $G = \lambda^2$, following Siegman (1966). The noise equivalent spectral radiance (NESR, in $\text{W m}^{-2} \text{sr}^{-1} \text{Hz}^{-1}$) is then simply.

$$NESR = \frac{NEP}{G \cdot B} \quad (5)$$

(in this study, it is expressed in $\text{mW m}^{-2} \text{sr}^{-1} (\text{cm}^{-1})^{-1}$).

The fixed value for the LHR throughput constrains the SNR; no improvement in SNR can be achieved by increasing the size of the FOV beyond the coherent limit. Conversely, the spatial footprint can be reduced without loss of SNR by increasing the collection optics aperture.

NWP systems typically assimilate data in units of brightness temperature, and are therefore used to express instrument noise as a noise equivalent delta temperature (NEdT, in K), following multiplication of the NESR by the inverse of the partial derivative of Planck's spectral radiance with respect to T :

$$\frac{dL_{\nu,T}}{dT} = \frac{2 \cdot h^2 \cdot \nu^4 \cdot e^{\frac{h\nu}{kT}}}{k \cdot c^2 \cdot T^2 \cdot \left(e^{\frac{h\nu}{kT}} - 1\right)^2} \quad (6)$$

where T is a blackbody reference temperature (280 K is often used for satellite interferometers), L is spectral radiance, and k is the Boltzmann constant. Figure 2 shows the LHR NEdT as a function of integration time, varying between 1 ms and

10 s, and of spectral resolution, varying between 30 MHz (0.001 cm^{-1}) and 3 GHz (0.1 cm^{-1}), at the shot-noise limit ($\rho = 1$), around 750 cm^{-1} , and for $T = 280 \text{ K}$.

Within the context of the information analysis following hereafter, the NESR is used for all calculations, and the noise model requires specification of the integration time per channel, τ , the spectral resolution (bandwidth) and the central wave number of the channel. The detector's heterodyne efficiency η is stipulated to be 0.5, and the degradation factor ρ set to a constant 1.0, which is based on an assumed ideal, shot noise-limited LHR.

Suitable values of integration time are affected by two major factors: the design of the LHR itself (scanning or multiplexing), and satellite viewing geometry, as discussed in sections 2 and 3.

5.3.2 | IASI noise covariance matrix

The performance of IASI is assessed using a diagonal instrument error covariance matrix of which the diagonal is shown in Figure 3, provided by the European Organisation for the Exploitation of Meteorological Satellites (EUMETSAT) via the eigenvector files used in their Level 1 principal component score data processing (these are described in EUMETSAT Document EUM/OPS-EPS/SPE/08/0195). The performance of IASI is in fact optimistic using the diagonal noise representation: calculations performed using a tri-diagonal instrument noise matrix that takes account of the inter-channel correlations introduced by apodisation (provided by Centre National d'Études Spatiales (CNES): Eric Pequignot, personal communication) produce lower information content by between 4 and 25%, depending on the channel selection. The results presented here are for the diagonal case, as it presents a higher benchmark for the LHR.

5.3.3 | Radiative transfer model error and errors of representation

Much of the error associated with the radiative transfer calculation, such as uncertainties in spectroscopic parameters or differences between fast model and line-by-line model, maps into a systematic error, or bias, rather than a random term. Another, possibly more important, source of error that should be incorporated into the observation error term during assimilation is the error of representation, in other words, horizontal or vertical scale mismatch between the observation and the NWP model grid.

For this study, RT model error and errors of representation are ignored, in other words we assume a perfect RT calculation, and a perfect mapping between model grid and observation spatial resolution. For the LHR, when combined with the perfect instrument assumption, the results presented here are therefore optimistic in terms of the impact on the NWP model. However, to compare possible LHR instrument configurations against each other, the assessment of RT and

scale mismatch errors is a secondary consideration for reasons outlined below.

It is justifiable to ignore RT errors because variability in the radiative transfer error within such a small portion of the spectrum as covered by an LHR is expected to be small, especially where absorbing gases are intentionally avoided. Secondly, for NWP applications, there would normally be some additional contribution from the use of a fast RT model, where parametrization often adds error over a line-by-line model. However, the errors of HT-FRTC relative to the well-known line-by-line model LBLRTM12.2 (Clough *et al.*, 2005) are very small for the $15\ \mu\text{m}$ CO_2 band (Havemann, 2015).

Representation or scale mismatch errors will indeed vary considerably depending on the precise application – in particular, they will depend on the grid size of the assimilating model. For an LEO LHR, mismatch will be high for a global model with a grid size of 10 km, but reasonably low for a convective-scale model with a sub-km grid. However, between LHR configurations on the same platform, they will be constant, and are therefore not critical in deciding which LHR configuration is best. There would be some variation between LEO and GEO platforms, because of the difference in footprint size, but for this preliminary study, the detail required to estimate representation error is not justified. NWP centres that assimilate data with correlated errors tend to use a diagnostic method to estimate the whole error covariance structure empirically (Desroziers *et al.*, 2005; Weston *et al.*, 2014). It is not easy to apply these methods to simulated data.

When comparing the LHR against IASI, it is important that we do not penalise IASI by incorporating more sources of error than were used for the LHR. Although it would be possible to use the operational error covariance matrix for IASI for the operational channels (derived using the Desroziers diagnostics) to ensure a consistent comparison, only the instrument error is used. Furthermore, a Desroziers diagnosis is not possible for channels that are not currently assimilated.

A drawback of this comparison is that errors of representation are likely to be different for the two instruments. The results of this study are optimistic, because it is clear that these other error terms are important contributions to the measured departures between observation and model forecasts (along with background errors). However, it is also clear that real IASI observations have a strong positive impact when assimilated in current NWP systems (Hilton *et al.*, 2012), so matching the information content from IASI in a controlled simulation is a sound indication that the LHR would also deliver benefits in the assimilation system on a per-observation basis.

5.4 | Profiles used to calculate Jacobians

Jacobians were calculated with HT-FRTC as described in section 5.1. The DFS was calculated as an average over eight atmospheric profiles on the 70 Met Office Unified Model (UM) levels, spanning a range of latitudes and atmospheric

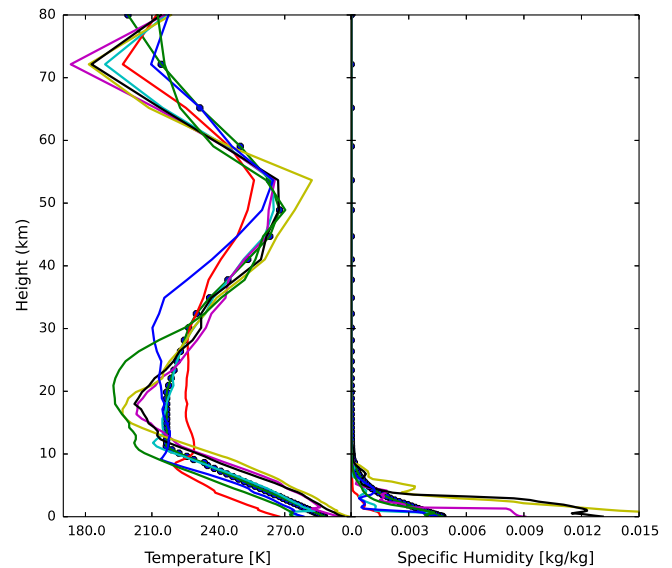


FIGURE 4 Plot of profiles used in the study. Each profile is plotted in a different colour. The US Standard Atmosphere is marked with blue circles [Colour figure can be viewed at wileyonlinelibrary.com]

TABLE 3 Average DFS for various IASI channel selections from Bands 1 and 2. The spectral range $645\text{--}720\ \text{cm}^{-1}$ is the long-wave CO_2 band where most of the temperature sounding channels are located

IASI Channel selection	Average DFS full profile	Average DFS above 6.8 km
The currently operational channel selection (listed in Hilton <i>et al.</i> , 2009b) from 645 to $1,900\ \text{cm}^{-1}$ (127 channels)	6.07	3.34
All channels from 645 to $1,900\ \text{cm}^{-1}$ (5,116 channels)	11.00	8.01
All channels from 645 to $720\ \text{cm}^{-1}$ (300 channels)	5.72	4.80
Operational Channel selection $645\text{--}720\ \text{cm}^{-1}$ (52 channels)	2.12	1.78

conditions. These profiles are plotted in Figure 4. Seven of the profiles are taken directly from the UM; the eighth is the US Standard Atmosphere. The same profiles were used for an IASI channel selection in Smith (2015). Where averaging kernels are shown below, they are for the US Standard Atmosphere.

6 | PERFORMANCE BENCHMARKING AGAINST IASI

For comparison with the LHR, the average DFS across the eight atmospheric profiles was calculated for a temperature retrieval using IASI Jacobians for a range of channel selections (Table 3). Since one of the proposed applications for the LHR is upper atmospheric sounding (investigated in section 7.6), the DFS for just the highest 40 levels of the UM (6.8–80 km; roughly 420 to 0.01 hPa) was also calculated. These results are also included in Table 3.

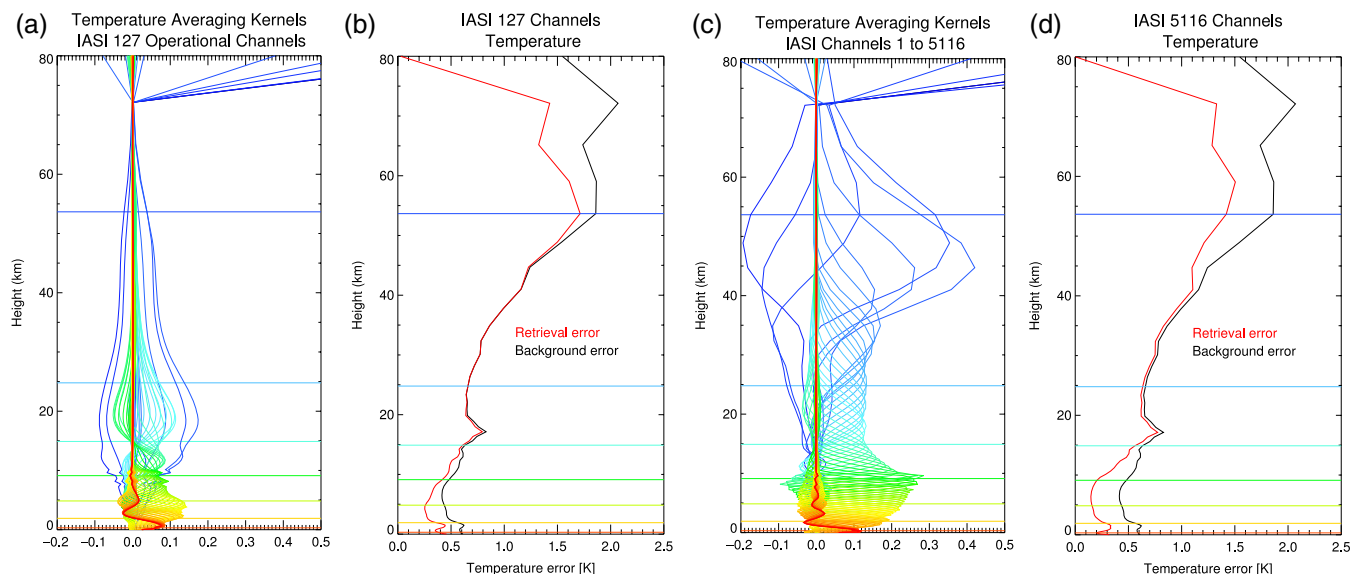


FIGURE 5 (a and b) Averaging kernels (a) and retrieval/background error comparison (b) for IASI for 127 operational channels. (c and d) Full spectrum to $1,900\text{ cm}^{-1}$. Every 10th model level is plotted as a horizontal line in the same colour as the kernel for that level, to aid interpretation [Colour figure can be viewed at wileyonlinelibrary.com]

The associated averaging kernels for the full profile retrieval for IASI for the two channel selections from the spectral range $645\text{--}1,900\text{ cm}^{-1}$ are shown in Figure 5. (Note that the averaging kernels for the topmost layer appear to contain an artefact from the radiative transfer model that incorrectly boosts the information content at these levels.) The operational channel selection strongly targets the troposphere. Inclusion of the full spectrum does add information above 35 km, with some channels providing information on a broad layer average temperature for the region 35–70 km, but the information remains primarily focused in the lower atmosphere.

7 | PERFORMANCE OF THE LHR FOR TEMPERATURE SOUNDING

7.1 | Initial spectral survey for microwindows

The aim of this study was to identify spectral windows that could be targeted by an LHR instrument for temperature sounding via CO_2 absorption lines. To be suitable for this task, there should be no contamination from water vapour (as the signal could alias between the two species), or from trace gases, including ozone. Many NWP centres, including the Met Office, do not currently have a sophisticated approach to simulating the effects of a varying ozone profile on the observed radiances.

For CO_2 , the spectral region around $13\ \mu\text{m}$ has been targeted, which is a small stretch from the readily available QCLs and photodiodes ($\sim 12.5\ \mu\text{m}$) but achievable through dedicated development. The full CO_2 band covers approximately $550\text{--}800\text{ cm}^{-1}$. The search for temperature sounding microwindows is kept to the short-wave side of 645 cm^{-1} in line with operational IR sounders.

Below 645 cm^{-1} , H_2O lines absorb significantly, and the contribution from the water vapour continuum can be 0.5 K or more.

The first step was to manually survey low-resolution simulations of an infrared spectrum between 645 cm^{-1} up to around $1,200\text{ cm}^{-1}$ (the short-wave end of the main water vapour absorption band) to find regions with strong CO_2 absorption lines, but few absorption lines for contaminating species, and weak absorption by contaminants. This process identified the most promising spectral region for temperature sounding to be $685\text{--}721\text{ cm}^{-1}$. The information content of an idealised LHR instrument with a spectral resolution of 0.001 cm^{-1} and an integration time of 25 s was assessed across this region. The DFS was calculated for 1 cm^{-1} (Advanced Multiplexing) and 0.1 cm^{-1} (Scanning and Multiplexing) microwindows across the spectral range, to find those with the most promising spectral features for sounding. The integration time was intentionally high, in order to ensure a very low contribution of instrument noise to the DFS, such that the differences in performance between microwindows could be isolated more easily. At this stage, therefore, the magnitude of the DFS is not representative of what the instrument can achieve.

The best microwindows will have maximum DFS but minimum contamination by interfering chemical species. A detailed survey of contaminants was undertaken using the US Standard Atmospheric profile, calculating absorption to the top of the atmosphere, using LBLRTM12.2, and assessing a standard contribution of all the gases referenced in the High-resolution Transmission molecular absorption (HITRAN) 2012 spectroscopic database (Rothman *et al.*, 2013), by removing them completely from the RT calculation, performing calculations at 0.001 cm^{-1} spectral resolution. Figure 6 shows the absorption lines of the only gases to have

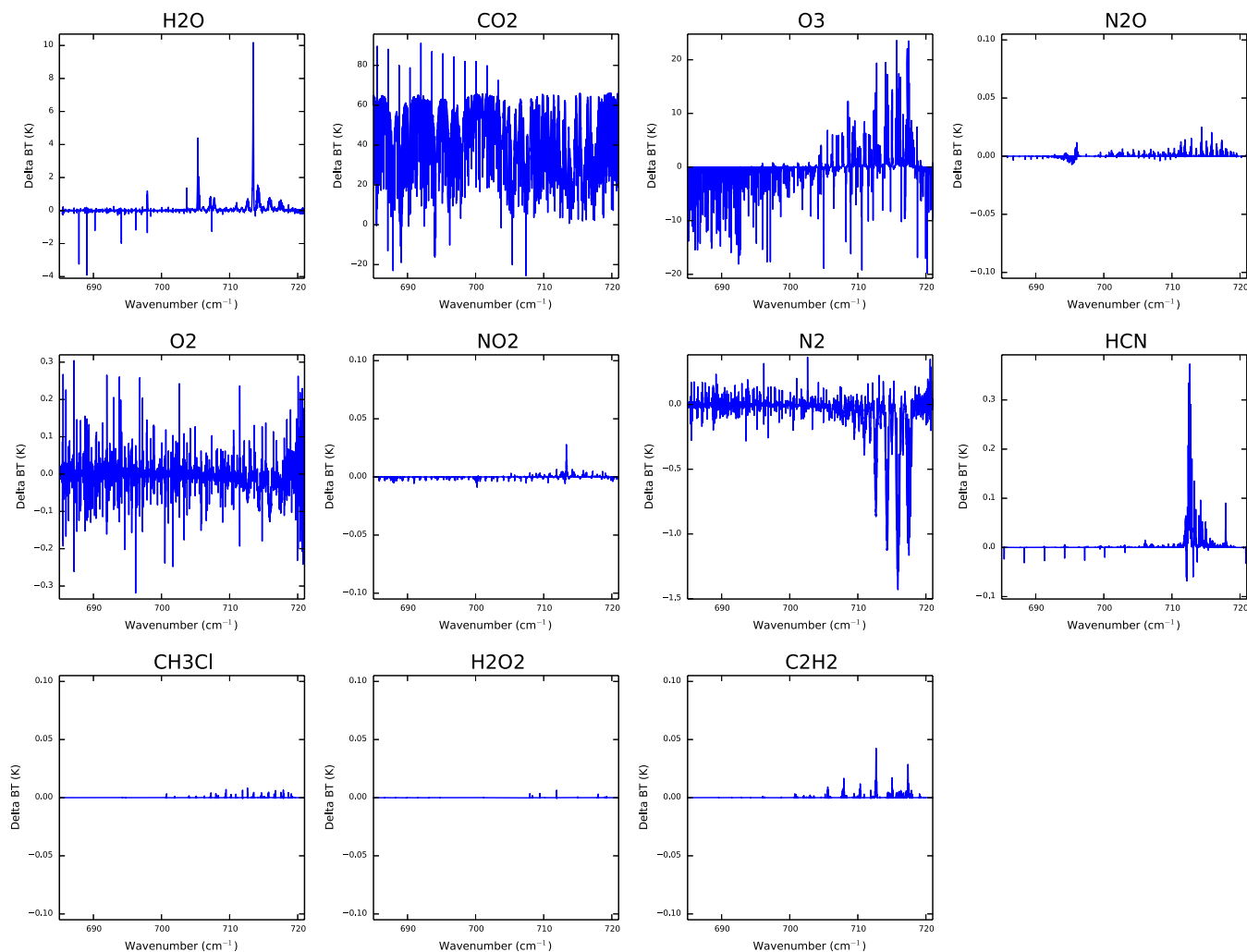


FIGURE 6 Gas absorption for the region 685–721 cm^{-1} (the range of the x -axis). The plotted quantity is the effect on the simulated brightness temperature of completely removing the gas from the simulation. Note that the y -axis range is variable. The only gases to have an effect bigger than 1 K at any frequency are H_2O , CO_2 , O_3 and N_2 [Colour figure can be viewed at wileyonlinelibrary.com]

significant absorption in this spectral region. Other than H_2O , CO_2 and O_3 , these are:

- O_2 and N_2 , which make up the bulk of the atmosphere, such that removing them will not give a realistic RT simulation. Given that they are well-mixed gases, they will in any case not cause problems for this application.
- HCN , for which absorption is limited to a spectral region between 710 and 715 cm^{-1} .
- N_2O , NO_2 , CH_3Cl , C_2H_2 and H_2O_2 , which have very small contributions below the 0.05 K level and can be ignored for the purposes of microwindow selection at this stage.

Figure 7 shows the DFS for Advanced Multiplexing 1.0 cm^{-1} microwindows at 0.001 cm^{-1} spectral resolution for 685–715 cm^{-1} , together with the maximum effect on brightness temperature from ozone, water vapour and other gas absorption that occurs in any part of each microwindow. The DFS is plotted at the start frequency of the microwindow. The spectrum from 715 to 720 cm^{-1} is more heavily contaminated by HCN and N_2 absorption lines, so was not

examined in detail, but 720.0–720.6 cm^{-1} was assessed (not shown). It appears that no microwindow is completely clear of ozone absorption. Two or three small regions where the ozone contribution is less than 5 K are visible between 700 and 705 cm^{-1} , but in all of these cases either the water vapour contamination is too high or the DFS is too low compared to other microwindows. Accepting significant ozone contamination, which tends to occur in isolated lines (see section 7.5), plenty of microwindows with minimal contamination by water vapour lines are available.

For 0.1 cm^{-1} microwindows (Scanning and Multiplexing modes), the DFS is much more variable but selectivity is enhanced, as expected from a narrower microwindow. As a result, regions with little interference from ozone are identifiable. Figure 8 is the same as Figure 7, but for 0.1 cm^{-1} microwindows. Only those microwindows with a DFS greater than 5 and contamination less than 1 K are shown. Many microwindows across the analysed spectral range appear suitable. Three promising regions, dense with appropriate microwindows, were selected for closer investigation for microwindows starting between:

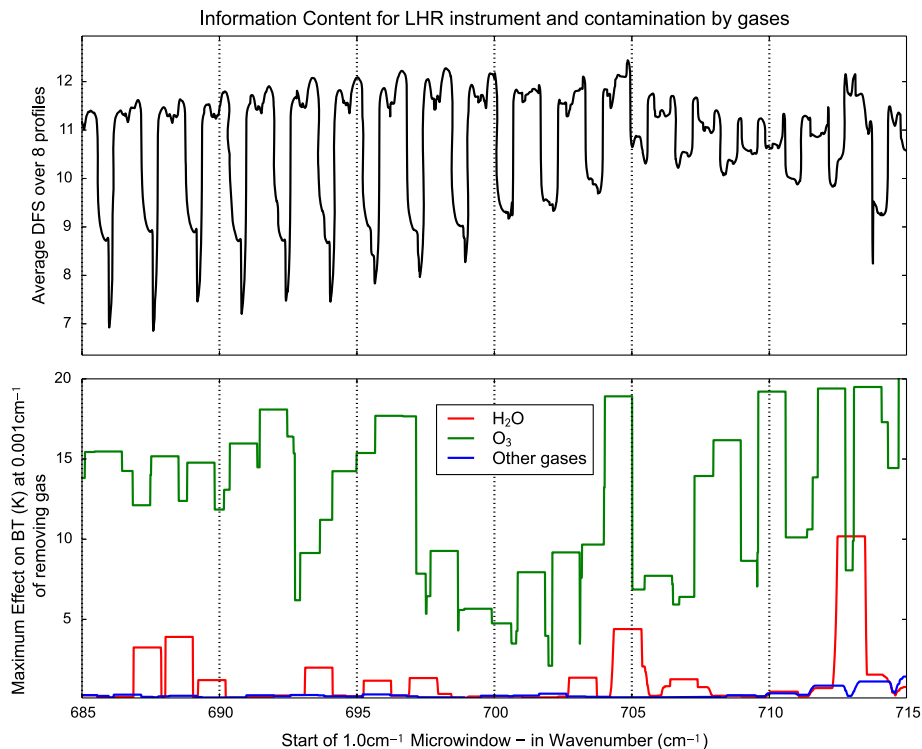


FIGURE 7 Average DFS (in black) for 1.0 cm^{-1} microwindows that start at a given wave number, and a hypothetical 25 s integration time. Below is the maximum effect of ozone absorption (green), water vapour absorption (red) and other gas absorption (blue) across the microwindow. The spectral range covered in this plot is $685\text{--}715 \text{ cm}^{-1}$. The spectrum from $715\text{--}720 \text{ cm}^{-1}$ is contaminated by HCN and N_2 absorption lines, so was not examined in detail. The range $720.0\text{--}720.6 \text{ cm}^{-1}$ was examined, but is not shown [Colour figure can be viewed at wileyonlinelibrary.com]

- 696.11 and 697.31 cm^{-1}
- 705.5 and 707.5 cm^{-1}
- 720.0 and 720.6 cm^{-1}

7.2 | Microwindow selection

The three regions selected above were scrutinized to locate the optimum microwindows for each proposed LHR configuration, using an integration time of 25 s per channel (note again that this integration time serves the purpose of selection only). Figure 9a shows, as an example, DFS and maximum contamination across the $705.5\text{--}707.5 \text{ cm}^{-1}$ spectral region for 0.1 cm^{-1} microwindows (Spectral Scanning mode or Multiplexing mode), at 0.005 cm^{-1} spectral resolution. It is possible to identify 0.1 cm^{-1} microwindows that minimize both ozone and water vapour contamination, whilst maximizing DFS.

Figure 9b shows the same information for 1.0 cm^{-1} microwindows (Advanced Multiplexing mode) with 0.005 cm^{-1} spectral resolution. The information content is higher for the 1.0 cm^{-1} microwindows, and less sensitive to the precise spectral location, because the spacing of the CO_2 absorption lines is such that it is generally possible to find at least one in a 1 cm^{-1} microwindow. For all spectral resolutions considered, the general pattern of regions of higher and lower DFS is the same, even though the location of the microwindow with the maximum DFS does vary.

For each of the three measurement modes, a microwindow with very high DFS and low contamination was selected in each of the promising spectral regions to conduct an analysis into the trade-offs between spectral resolution, microwindow width and integration time. For ease of comparison, the microwindow was not changed when the influence of spectral resolution was studied (eventually a microwindow re-optimization will be needed if the best window is to be selected for future studies). For Multiplexing and Advanced Multiplexing modes, DFS calculations were performed for the three listed acquisition times: 0.15, 1.0 and 5.0 s. In every measurement mode and for a given spectral resolution, DFS is highest with the longest acquisition time, as this improves the noise performance considerably. In Spectral Scanning mode, different sampling resolutions were considered for an acquisition time of 5.0 s. Table 4 summarizes these DFS results.

7.3 | Performance in Spectral Scanning mode

Recall that in Spectral Scanning mode, each channel is measured successively, meaning that the integration time is a fraction of the total acquisition time that depends on the sampling resolution of the instrument. In general, the integration time is extremely short, which has a large detrimental impact on the NEdT.

The integration time can obviously be increased with longer acquisition times, but also by reducing the measurement's spectral resolution from the highest achievable, or by

Information Content for LHR instrument and contamination by gases
Only microwindows with high DFS and low contamination are shown

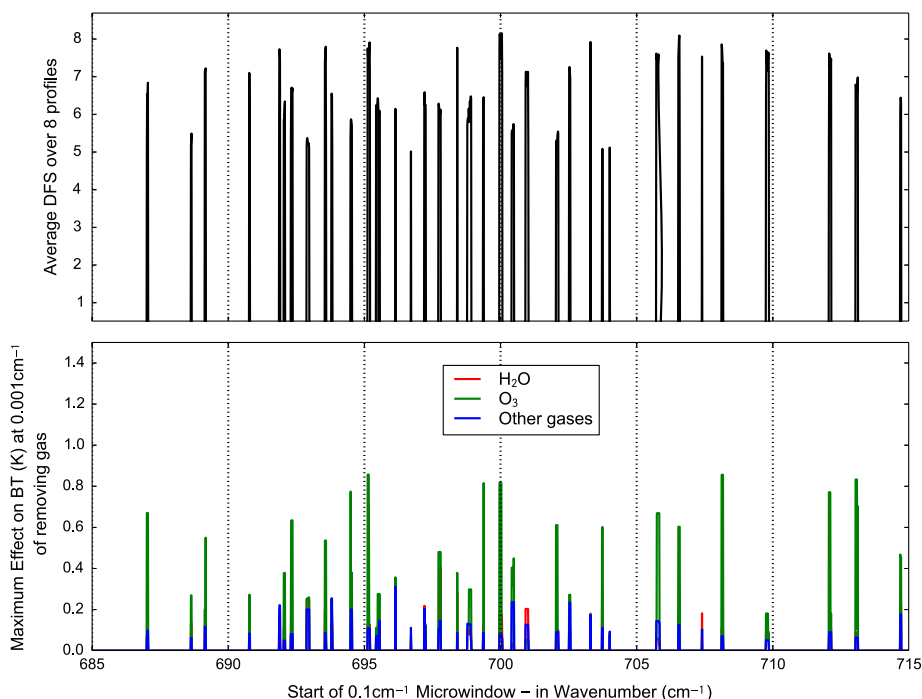


FIGURE 8 Same as Figure 7, but for 0.1 cm^{-1} microwindows (note change of y-axis scale). Only microwindows where the average DFS >5.0 and the maximum contamination from any gas $<1.0 \text{ K}$ are shown [Colour figure can be viewed at wileyonlinelibrary.com]

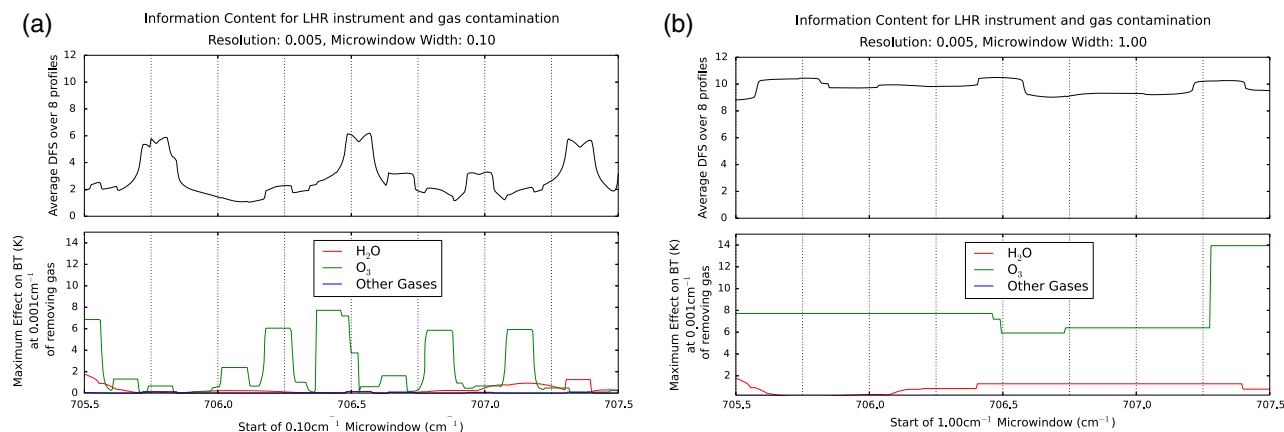


FIGURE 9 Average DFS for 0.1 and 1.0 cm^{-1} microwindows, with maximum absorption from other species. (a) Scanning/Multiplexing 0.005 , (b) Advanced Multiplexing 0.005 [Colour figure can be viewed at wileyonlinelibrary.com]

reducing the sampling resolution (spectral under-sampling). Individual channels need not be contiguous. For example, with a spectral resolution of 0.001 cm^{-1} , using a step-function for the laser current, successive samples could instead be spaced by e.g. 0.002 cm^{-1} , 0.004 cm^{-1} , etc. These options to improve the instrument's noise performance were investigated. Although they made quite a difference, the best performing instrument still has an NEdT at 280 K of around 0.7 K (NESR $0.8 \text{ mW m}^{-2} \text{ sr}^{-1} (\text{cm}^{-1})^{-1}$). For comparison, at these wave numbers, IASI's NEdT is around 0.18 K . Furthermore, even though reducing the sampling resolution improves the noise, this does not necessarily translate into a higher DFS, because important spectral features can be missed by the coarser sampling.

The poor noise performance at these short integration times associated with the very high spectral resolution, coupled with the limited width of the microwindow, means that the DFS is very small. The best performing instrument (sampling 0.002 cm^{-1} -wide channels every 0.008 cm^{-1} ; i.e. 13 channels for the microwindow at 720.434 cm^{-1}), gives a DFS of only 0.85 , i.e. less than one piece of information, and not even enough to estimate a column average. In summary, Spectral Scanning mode is unsuitable for NWP.

7.4 | Performance in Multiplexing mode

In Multiplexing mode, acquisition time is equal to integration time. This means that for a 5 s integration time, a

TABLE 4 Information content for idealized LHR instruments

Mode	Instrument lower bound (cm ⁻¹)	Measurement resolution (cm ⁻¹)	Sampling resolution (cm ⁻¹)	Number of channels	Integration time, τ (s)	NESR (mW m ⁻² sr ⁻¹ (cm ⁻¹) ⁻¹)	Average DFS (full profile)
SSM	696.117	0.002	0.002	50	0.10	1.641	0.43
SSM	706.568	0.002	0.008	13	0.38	0.875	0.61
SSM	720.434	0.002	0.008	13	0.38	0.927	0.85
MM	706.570	0.005		20	0.15	0.886	0.7
MM	706.570	0.005		20	1	0.343	2.3
MM	706.570	0.005		20	5	0.153	4.4
MM	720.500	0.005		20	0.15	0.939	0.8
MM	720.500	0.005		20	1	0.364	2.3
MM	720.500	0.005		20	5	0.163	3.7
AMM	696.260	0.002		500	0.15	1.341	3.1
AMM	696.260	0.002		500	1	0.519	6.6
AMM	696.260	0.002		500	5	0.232	9.1
AMM	705.760	0.002		500	0.15	1.396	2.6
AMM	705.760	0.002		500	1	0.541	6.0
AMM	705.760	0.002		500	5	0.242	8.9
AMM	720.220	0.002		500	0.15	1.484	3.3
AMM	720.220	0.002		500	1	0.575	6.5
AMM	720.220	0.002		500	5	0.257	9.1
AMM	696.260	0.02		50	0.15	0.424	2.3
AMM	696.260	0.02		50	1	0.164	4.82
AMM	696.260	0.02		50	5	0.073	6.83
AMM	705.760	0.02		50	0.15	0.441	1.77
AMM	705.760	0.02		50	1	0.171	4.16
AMM	705.760	0.02		50	5	0.076	6.41
AMM	720.220	0.02		50	0.15	0.469	1.88
AMM	720.220	0.02		50	1	0.182	4.18
AMM	720.220	0.02		50	5	0.081	6.41

Note. In Spectral Scanning mode (SSM), all instruments have an acquisition time of 5 s and a microwindow of 0.1 cm⁻¹. In Multiplexing mode (MM), instruments have 0.1 cm⁻¹ microwindows, and the same acquisition time as τ . Advanced Multiplexing mode instruments (AMM) have 1.0 cm⁻¹ microwindows and the same acquisition time as τ . Values that match IASI DFS are shown in italics.

good NESR of around 0.15 mW m⁻² sr⁻¹ (cm⁻¹)⁻¹ can be achieved, equivalent to 0.1 K NEDT at 280 K. This is in line with state-of-the-art performance in operational IR hyperspectral sounders. Two spectral resolutions were considered (0.005 and 0.01 cm⁻¹). The DFS was similar for the two spectral resolutions but the higher spectral resolution instruments had a marginally higher DFS in each microwindow.

Referring to Table 4, performance at 0.15 s integration time is too poor to make an LHR of that type useful for NWP. Even at 1 s, there are only around 1–2 pieces of information available for the full 70-level temperature profile. With 5 s available to make the measurements, this number increases to more than 3 pieces of information for two of the microwindows; still not enough to provide any kind of a profile. If, however, the instrument could be optimised such that the 3 pieces of information were to be located in the very highest levels of the atmosphere, it might be worth considering, as there are few other observations of the uppermost atmosphere. Section 7.6 explores microwindows for a dedicated upper-atmosphere mission.

7.5 | Performance in Advanced Multiplexing mode

Advanced Multiplexing mode differs from Multiplexing mode only in that it has a wider microwindow of 1.0 cm⁻¹. In this case, however, as we considered future technology, an extended range of spectral resolutions was explored. Table 4 shows the performance of the Advanced Multiplexing modes, for spectral resolutions of 0.002 and 0.02 cm⁻¹, which were the highest and lowest values examined.

The average DFS is much higher for Advanced Multiplexing mode than for Multiplexing mode, because of the wider microwindow. The higher spectral resolutions give a higher DFS, but even at 0.02 cm⁻¹, instruments with a DFS competitive with IASI are possible. At resolutions higher than 0.005 cm⁻¹, mounting on an LEO platform in push-broom configuration also becomes viable, with over 6 pieces of information per profile at a 1 s integration time. Performance on a cross-track scanner (0.15 s) is still marginal with around 3 pieces of information at the highest spectral resolution. These results are promising, suggesting that as multiplexing

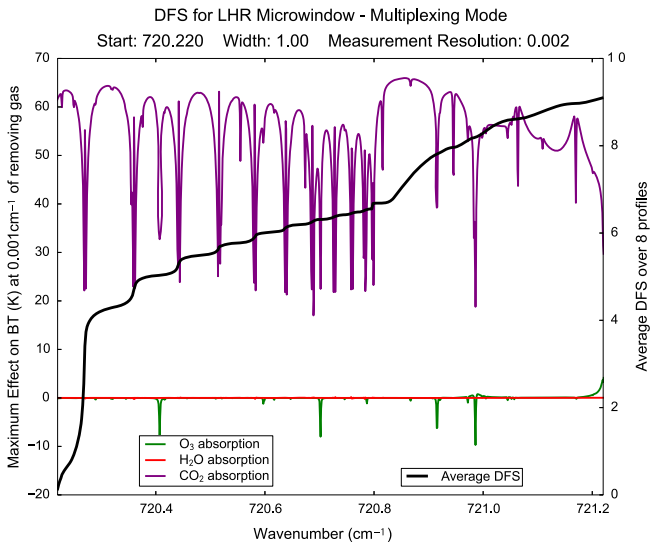


FIGURE 10 Absorption lines for CO₂ (purple), H₂O (red) and O₃ (green) plotted across an optimised Advanced Multiplexing 1.0 cm⁻¹ microwindow starting at 720.220 cm⁻¹. The DFS increase for each additional channel of the microwindow, calculated with a 5 s integration time, is plotted with a thick black line [Colour figure can be viewed at wileyonlinelibrary.com]

options improve, the LHR could be a viable instrument for application in NWP.

Figure 10 shows the increase in DFS across one of the chosen microwindows (720.22 cm⁻¹) for the Advanced Multiplexing 0.002 cm⁻¹ instrument with a 5 s integration time, as each additional channel is added, overlain by the spectral absorption features in the microwindow. There is an increase in information content as channels that sample the centre of a new CO₂ absorption line are added. Not all absorption lines appear to add new information, for example, the line at 721.0 cm⁻¹. The reason for this is not currently known but could relate to the coincident ozone lines.

Although it is not possible to avoid ozone contamination across the whole microwindow, the absorption features are very sharp. At 0.002 cm⁻¹ spectral resolution, there will be 500 channels in a microwindow. The channels sensitive to ozone could easily be dropped for assimilation via a standard channel selection mechanism, probably without a significant change in the information content, since in most cases these channels do not coincide with a portion of the microwindow where the DFS is increasing sharply.

Figure 11 shows the averaging kernels for the same microwindow, along with the error in the retrieved temperature profile. Comparison with the result for IASI (Figure 5) shows that the LHR is providing complementary information above 20 km.

7.6 | Performance for upper-atmospheric temperature sounding

Given that the IASI averaging kernels are so heavily weighted towards sounding the lower atmosphere, the most promising application for the LHR instrument would be to sound the uppermost levels of the atmosphere, where there are

presently few observations. In the stratosphere, the horizontal length-scales of temperature variation are long enough that an observation offering relatively sparse spatial sampling and/or with a relatively large footprint along-track could prove to be beneficial. Thus, retaining a short integration time on a LEO-mounted instrument is less critical, opening possibilities for point-and-stare viewing mode. This section explores targeting microwindow selection for the upper atmosphere.

In order to find the best microwindow for upper-atmosphere sounding, the selection process was altered to choose the best frequencies for sounding in the top 40 levels of the UM, spanning 6.8–80 km (roughly 420–0.01 hPa). Table 5 shows the DFS for the best-performing Multiplexing and Advanced Multiplexing modes evaluated in terms of the DFS over these levels.

Figure 12 shows the increasing DFS across a 1.0 cm⁻¹ Advanced Multiplexing 0.002 cm⁻¹ upper atmosphere-optimised microwindow. The DFS increases most rapidly as the wing of the extremely strong absorption line the signal from lower layers of the atmosphere; the sharp increase in DFS is the result of a channel near the centre of the line enabling a previously unsampled very high layer of atmosphere to be measured. The high spectral resolution allows the contribution from the very narrow region close to the centre of the line to be resolved.

Both Multiplexing and Advanced Multiplexing modes give high information content for the upper atmospheric layers, and consequently, the associated vertical resolution is high, as can be seen in the averaging kernels (Figure 13). For the Advanced Multiplexing mode instrument, the sounding is restricted to levels above 6 km, and for the 0.1 cm⁻¹ Multiplexing Mode instrument, there is no contamination from below 17 km. In these plots, the averaging kernels are plotted for the full profile retrieval; although the microwindows were chosen for information content using DFS over the top 40 levels only, it turns out that these microwindows are in any case free from contamination from the lower atmosphere. Even with 1 s integration time, the DFS of a Multiplexing Mode instrument is reasonable. Therefore, the LHR holds great promise in this area, seeming to provide novel measurements that are complementary to those from sounders focusing on the lower atmosphere.

8 | INSTRUMENT TRADE-OFFS

The previous section established a first picture of the potential of the LHR for NWP and identified the most promising applications. In this section, trade-offs between different aspects of the instrument design are discussed in more detail.

8.1 | Microwindow width

The choice of a 1.0 cm⁻¹ microwindow in Advanced Multiplexing mode is somewhat arbitrary. A smaller

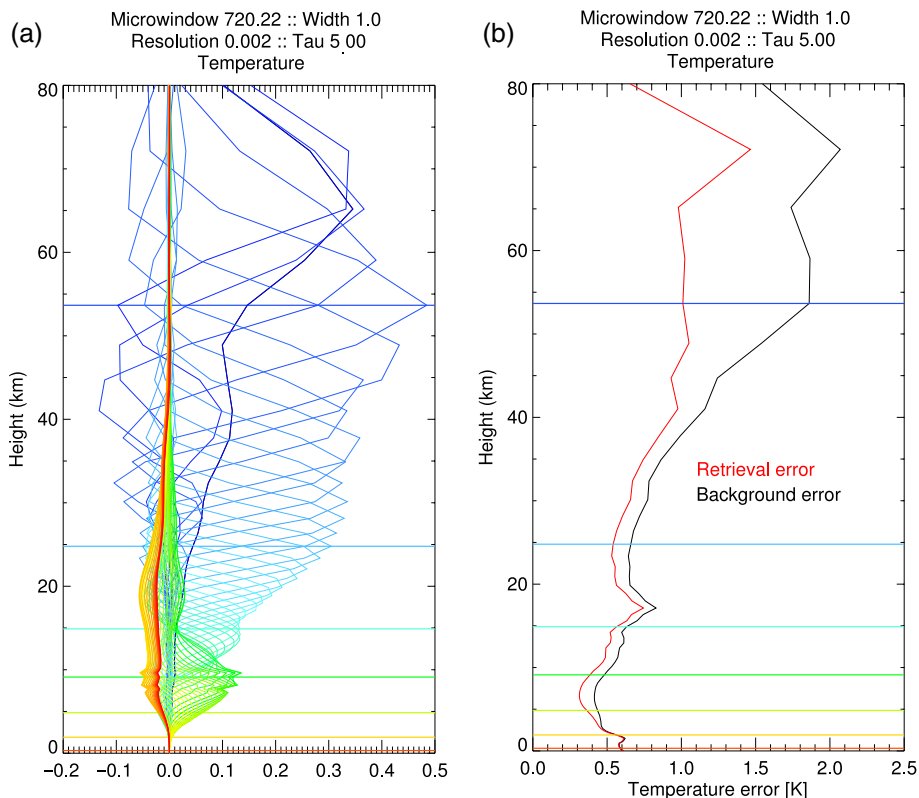


FIGURE 11 (a) Averaging kernels and (b) retrieval/background error comparison, for the Advanced Multiplexing 0.002 retrieval at 720.22 cm^{-1} with 0.002 cm^{-1} resolution and a 5 s integration time. Every 10th model level is plotted as a horizontal line in the same colour as the kernel for that level, to aid interpretation [Colour figure can be viewed at wileyonlinelibrary.com]

TABLE 5 Upper-atmosphere information content for Multiplexing and Advanced Multiplexing (0.1 and 1 cm^{-1}) microwindows optimised for upper-air sounding (same acquisition time as τ)

Instrument lower bound (cm^{-1})	Measurement resolution (cm^{-1})	Number of channels	Integration time, τ (s)	NESR ($\text{mW m}^{-2}\text{ sr}^{-1}(\text{cm}^{-1})^{-1}$)	Average DFS
Multiplexing mode					
693.580	0.005	20	5	0.145	5.2
693.580	0.005	20	1	0.325	3.5
691.890	0.01	10	5	0.102	4.5
691.890	0.01	10	1	0.288	3.1
Advanced multiplexing mode					
<i>692.820</i>	<i>0.002</i>	<i>500</i>	<i>5</i>	<i>0.229</i>	<i>9.4</i>
<i>692.825</i>	<i>0.005</i>	<i>200</i>	<i>5</i>	<i>0.145</i>	<i>8.9</i>
<i>692.830</i>	<i>0.01</i>	<i>100</i>	<i>5</i>	<i>0.102</i>	<i>8.0</i>
<i>692.840</i>	<i>0.02</i>	<i>50</i>	<i>5</i>	<i>0.072</i>	<i>7.3</i>

Note. Values that exceed IASI upper atmosphere DFS are shown in italic.

microwindow (0.8 cm^{-1} , for example) would be cheaper, and could suffice depending on the application. Examining the increase in DFS across a 1.0 cm^{-1} microwindow, as shown in Figures 10 and 12, we see that the DFS increases more sharply across certain parts of the microwindow, depending on the locations of the main absorption features. On the other hand, each additional channel does bring an incremental amount of information to the retrieval, which does not necessarily plateau (for example, the DFS is still increasing steadily at the end of the microwindow in Figure 10).

Because of the strong dependence on specific absorption features, it is difficult to establish a generic optimal microwindow width. Associated trade-offs should be analysed once appropriate photomixers are more mature, the technology has been demonstrated, and the target application is better specified. On the other hand, there are certain benefits to restricting the instrument to a narrow microwindow; for example, for an upper-atmosphere mission, where, a wide microwindow appears not to be strictly necessary, a narrow window provides the benefit of avoiding sensitivity to the lower atmosphere.

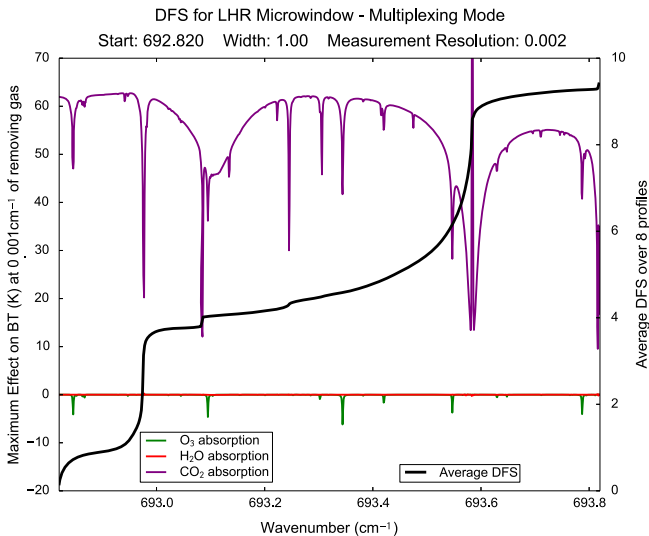


FIGURE 12 Same as Figure 10 (with 5 s integration time), but for a microwindow starting at 692.82 cm^{-1} , optimised for upper-atmosphere sounding [Colour figure can be viewed at wileyonlinelibrary.com]

8.2 | Spectral resolution

In general, increasing the spectral resolution improves the information content, despite the increasing noise (compare numbers at 0.002 cm^{-1} resolution with those at 0.02 cm^{-1} resolution for Advanced Multiplexing mode in Table 4). Figure 14 shows the averaging kernels at four different spectral resolutions (0.002 , 0.005 , 0.01 and 0.02 cm^{-1}) in Advanced Multiplexing mode, for a microwindow at 705.76 cm^{-1} and 5 s integration time. These plots show that the main impact of reducing the spectral resolution is to reduce the vertical resolution of the retrieval in the upper atmosphere, as spectral features associated with the narrowest line width emission (i.e. lowest pressures) are no longer resolved. Where possible, the highest spectral resolution feasible should thus be chosen, particularly for an upper-atmospheric sounding instrument.

8.3 | Integration time

The results in section 7 show that the effects of integration time on instrument noise and consequently on information content are very high. For temperature sounding in the $13 \mu\text{m}$ region of the CO_2 band, an LEO cross-track scanning LHR is not feasible, nor is an instrument in Spectral Scanning mode, because the acquisition time is too short to allow for sufficient integration time for reducing the noise.

Figure 15 shows the impact of decreasing the integration time from 5 to 1 to 0.15 s in Advanced Multiplexing 0.002 cm^{-1} mode at 705.76 cm^{-1} . Whilst the overall information content drops dramatically (from 8.9 to 6.0 to 2.6) as the integration time is reduced, the shape of the averaging kernels also changes significantly. In particular, the information content below 30 km drops to near zero by 0.15 s, but there remains some information content aloft, albeit with poor vertical resolution. This is almost certainly because the

upper-atmospheric levels are more poorly modelled by the UM relative to the mid- to lower troposphere, so the background errors are larger and noisy observations still have some value. This suggests that if integration time is restricted, it is certainly worth focusing on an upper-atmospheric sounder to provide novel measurements for NWP.

8.4 | Trade-off conclusions

Unsurprisingly, the ideal instrument that offers the best flexibility in sounding applications would have the widest microwindow with the highest spectral resolution possible, and the longest integration time. However, these parameters are not independent, and must realistically be traded off in line with space-borne LHR mission objectives.

Some of the scenarios analysed rely on prospective technology advances, particularly in terms of spectral multiplexing. Optimal combinations of microwindow width and spectral resolution should be revisited as the technology develops. Nevertheless, there are already indications as to which type of instrument would contribute most to NWP. The results presented in section 7.6 indicate that, for a dedicated stratospheric sounding mission, a recommendation of high spectral resolution over a wide microwindow could be made. A Multiplexing mode instrument (with a 0.1 cm^{-1} microwindow) operating at high spectral resolution (0.001 cm^{-1}) would be a good candidate for an in-orbit demonstration of a stratospheric sounding mission from a small satellite platform.

Conversely, as stated in section 7.5, a wide microwindow can provide useful information on broad layers of the upper atmosphere even at lower spectral resolution. It seems reasonable to recommend, for a full-atmosphere sounding mission, that a wide microwindow should be prioritised over high spectral resolution.

With an integration time of 5 s, the noise performance of the LHR is acceptable in either Multiplexing or Advanced Multiplexing mode. Such an instrument could target either a GEO platform, or an LEO satellite with a point-and-stare instrument. For GEO platforms, further work is needed to optimise a viewing configuration; although targeted sounding has been mooted in the context of examining severe weather features such as hurricanes, it is not clear how useful this type of configuration would be for an upper-atmosphere sounder. A sparse full-disk scanning mode might be preferable.

A LEO point-and-stare configuration seems plausible for an upper-atmosphere sounder, given that the atmosphere is smoother in structure in the stratosphere, and that the general lack of existing observations means that sparse measurements can still add information to the NWP model. For tropospheric sounding, where spatial information is more critical, a lack of cross-track measurements would certainly limit the impact of an LHR, given a global observing system already saturated with hyperspectral IR sounding missions with wide spatial coverage from both LEO and GEO platforms.

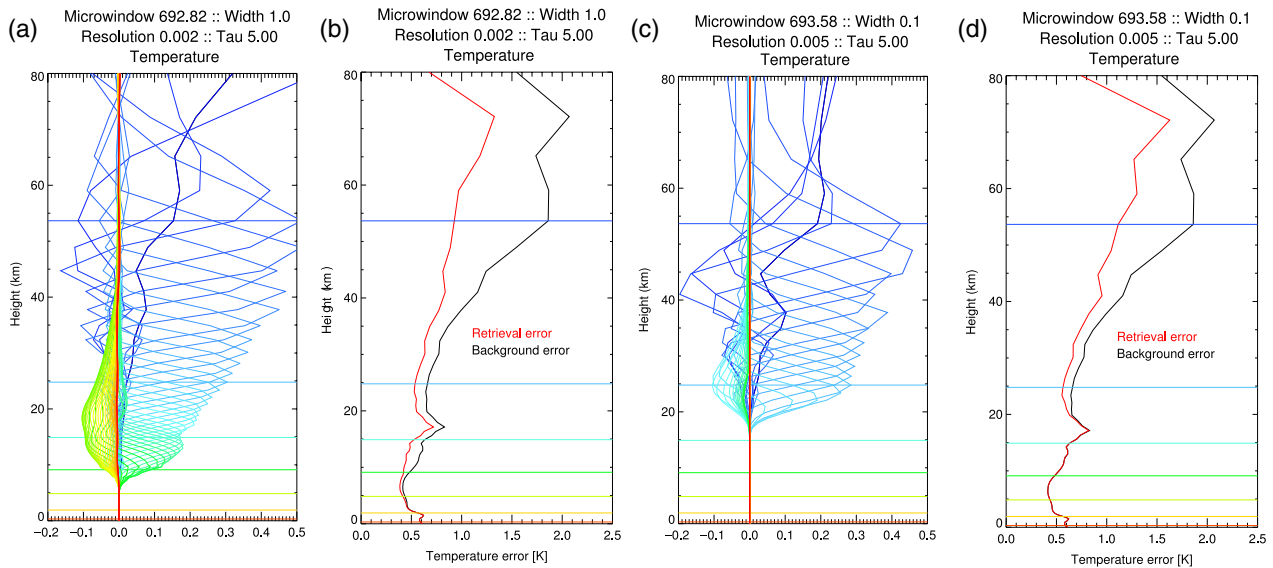


FIGURE 13 Same as Figure 11 (with 5 s integration time), but optimised for upper-atmosphere sounding; (a, b) in Advanced Multiplexing mode with 0.002 cm^{-1} resolution, and (c, d) in Multiplexing mode with 0.005 cm^{-1} resolution [Colour figure can be viewed at [wileyonlinelibrary.com](#)]

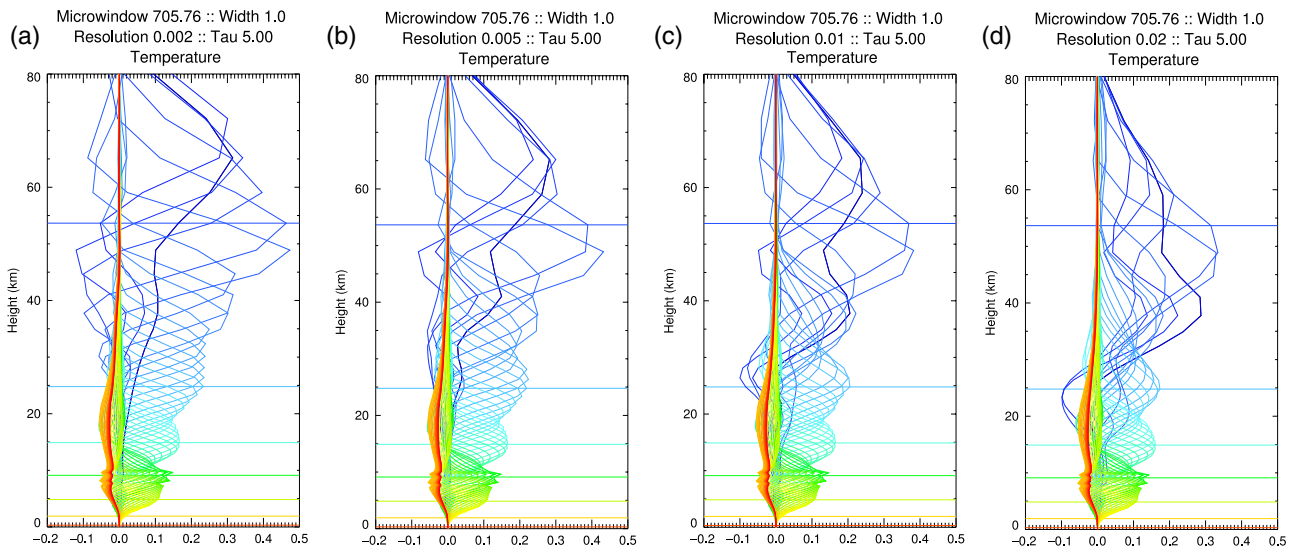


FIGURE 14 Averaging kernels for a 1.0 cm^{-1} microwindow at 705.76 cm^{-1} with 5 s integration time, for four different spectral resolutions (a–d): 0.002, 0.005, 0.01 and 0.02 cm^{-1} . Every 10th model level is plotted as a horizontal line in the same colour as the kernel for that level, to aid interpretation [Colour figure can be viewed at [wileyonlinelibrary.com](#)]

9 | FUTURE DIRECTIONS

A secondary aim of this study was to identify other areas where the LHR may contribute, and thus further study is merited. Two areas were considered: water vapour sounding and mesospheric temperature sounding.

9.1 | Water vapour sounding

In the $6\text{ }\mu\text{m}$ water vapour band, which is traditionally used for water vapour sounding by infrared satellite instruments, the noise performance of the LHR would be very poor at all realistic acquisition times for a nadir-viewing instrument (NESR of $1.2\text{ mW m}^{-2}\text{ sr}^{-1}\text{ (cm}^{-1}\text{)}^{-1}$ at 5 s integration time, giving an NEDT of 2.9 K, compared with around 0.2 K for IASI).

This leads to extremely low DFS, and optimal instrument configurations were not pursued.

Given the relatively unpromising results in the main water vapour band, an initial survey of the prospects of water vapour sounding below 600 cm^{-1} was undertaken. At long wavelengths between 500 and 600 cm^{-1} (16.7 to $20\text{ }\mu\text{m}$), the noise performance of the LHR is excellent (NESR of $0.06\text{ mW m}^{-2}\text{ sr}^{-1}\text{ (cm}^{-1}\text{)}^{-1}$, or NEDT of around 0.1 K for an integration time of 1 s at 0.005 cm^{-1} resolution), and there is strong water vapour absorption but little contamination from trace gases. Initial calculations with the existing **B** matrix gave extremely high DFS of 35–45 for Advanced Multiplexing and 10–20 for Multiplexing mode instruments.

The averaging kernels for these instruments show that the information is highly concentrated above 4.5 km, which

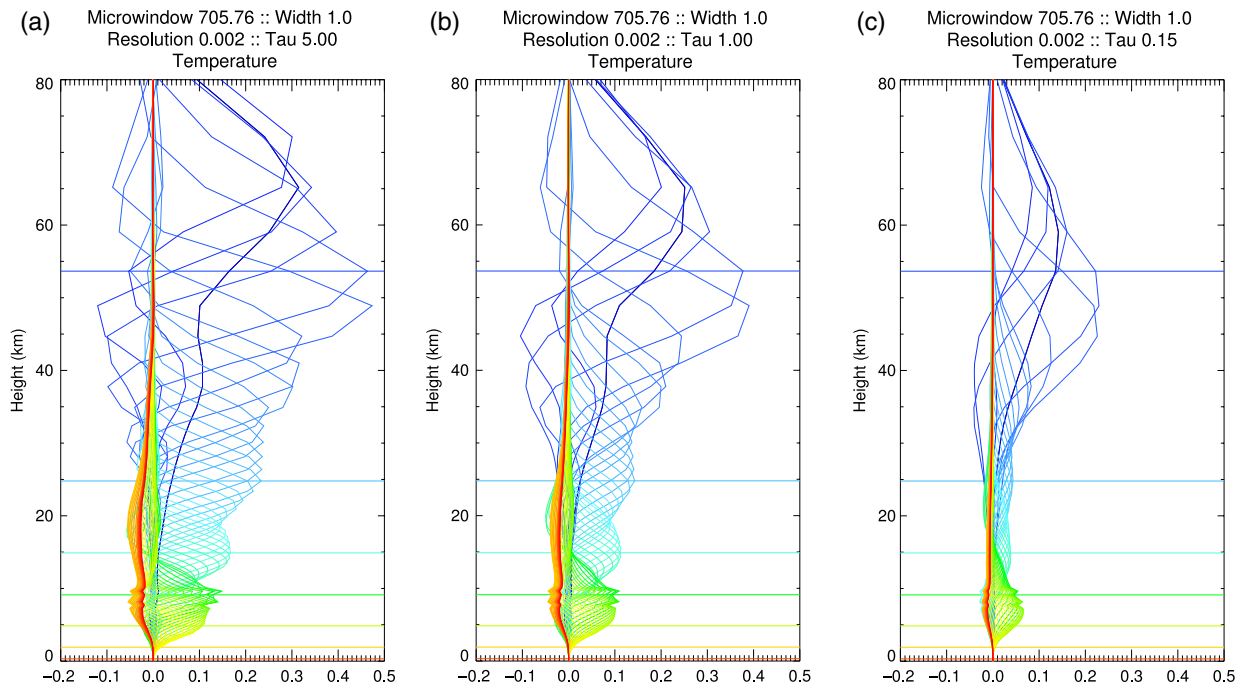


FIGURE 15 Averaging kernels for a 1.0 cm^{-1} microwindow at 705.76 cm^{-1} with 0.002 cm^{-1} spectral resolution, for decreasing integration time (a–c: 5, 1, and 0.15 s). The associated DFS are 8.9, 6.0 and 2.6 respectively [Colour figure can be viewed at wileyonlinelibrary.com]

immediately raises concerns about the validity of the **B** matrix. The 4D-Var error covariance statistics are derived through analysis of an ensemble of model fields. Since the water vapour content of the stratosphere is extremely low, and there are no observations to constrain the model, the relative errors in the fields will be very large. Although using the logarithm of the mixing ratio protects to a certain extent against this, it is extremely unlikely that the 4D-Var covariance statistics will be at all reliable in this region. In consequence, the 1D **B** matrix is not well-enough constrained to deliver reasonable DFS results. However, what can be said from these initial results is that there is clearly information on the upper atmospheric water vapour profile at these wavelengths, and this application certainly merits further investigation.

One other thing to note is that in Multiplexing mode, the DFS for water vapour sounding was very insensitive to integration time. Thus, if the high information content predicted by this study can be confirmed with more realistic background errors, the LHR could target an LEO platform as a cross-track scanner.

From a technology standpoint, whilst the results look very promising, a significant level of technological development is required to produce suitable single-mode continuous wave QCLs operating in the far IR, along with the associated photomixers.

9.2 | Mesosphere temperature sounding

One other possible application is mesospheric temperature sounding. Studying the information content in this part of the atmosphere is not easy: the Met Office's UM currently has only six levels between 50 and 80 km, and the background

error covariance model is not optimised for the topmost levels. Although a test configuration exists with a higher vertical resolution, there are currently no plans to extend the model top beyond 80 km, though space weather models typically start at 100 km. Nevertheless, it would be interesting to target these uppermost levels of the atmosphere, as there is a definite gap in observations that can anchor the temperature there. The mission could also link Earth and space weather as a prime objective.

Another future mission study could be limb sounding for upper atmospheric temperature. Many upper-atmospheric instruments on LEO platforms are limb-sounders, which provide high vertical-resolution information of the upper levels, albeit with low horizontal resolution (as previously mentioned, low horizontal resolutions are less important at the longer horizontal length-scales in the upper atmosphere). Although NWP models typically do not yet assimilate data from IR limb sounders, RT models exist (such as RFM: Dudhia, 2016) that have the relevant forward modelling capability, and there have been studies into the use of 2D operators for instruments such as GNSS-RO (Global Navigation Satellite System Radio Occultation).

10 | CONCLUSIONS AND OUTLOOK FOR THE LHR IN NWP

The main aim of this study was to assess whether a laser heterodyne radiometer, measuring in narrow spectral microwindows ($0.1\text{--}1.0 \text{ cm}^{-1}$) at very high spectral resolutions ($0.001\text{--}0.01 \text{ cm}^{-1}$) could provide useful additional information on atmospheric temperature for NWP applications. The

baseline performance targeted is that achieved by current interferometric radiometers (IASI) operating at moderately high resolution (0.25 cm^{-1}) and spanning the whole of the mid-infrared region of the spectrum ($645\text{--}2,760\text{ cm}^{-1}$).

The study ruled out the following configurations of the LHR as feasible candidate missions:

- For the necessarily short acquisition times appropriate for a cross-track scanning nadir sounder from low Earth orbit (0.15 s for IASI), the noise levels achievable by the LHR are insufficiently low for the LHR to be a candidate.
- For an LHR in Spectral Scanning mode, where each channel is measured sequentially, with narrow 0.1 cm^{-1} microwindows and a 5 s total acquisition time, NEdT values are around 0.7 K (in contrast to IASI which has an NEdT of 0.18 K for a 0.15 s acquisition time), resulting in low DFS. The study therefore concluded that the LHR could not be used in Spectral Scanning mode.

However, the study found promising results for the LHR in NWP under the following conditions:

- In Multiplexing mode, with currently achievable intermediate frequencies (IFs) in the range 0–3 GHz, the LHR offers marginally viable full-profile sounding for optimised microwindows of 0.1 cm^{-1} width at resolutions of $0.005\text{--}0.01\text{ cm}^{-1}$ and for integration times of 5 s, plausible for geostationary satellites or for a point-and-stare LEO mission.
- The Advanced Multiplexing mode, requiring intermediate frequencies in the range 0–30 GHz, enabled useful information on temperature to be obtained for microwindows of 1 cm^{-1} width and integration times of 1 s, consistent with LEO deployment in a push-broom configuration. DFS values were acceptable for all spectral resolutions considered. For integration times of 5 s (GEO or point-and-stare deployment), very competitive DFS values of 9.1 were obtained for a spectral resolution of 0.002 cm^{-1} . This is higher than that obtained with the operational IASI channel selection.
- The LHR offers very competitive performance for temperature sounding throughout the stratosphere and lower mesosphere. Microwindows of 1.0 cm^{-1} width optimised for upper atmospheric temperature sounding, with an integration time of 5 s, gave DFS values of 7.3–9.4 for the top 40 levels of the Met Office's Unified Model (spanning 6.8–80 km, roughly $420\text{--}0.01\text{ hPa}$). These compare favourably with 3.3 for the operational IASI channel selection, and 8 for the full spectrum from $645\text{ to }1,900\text{ cm}^{-1}$. On the other hand, narrow 0.1 cm^{-1} microwindows yield DFS values of 4.5–5.2 while also enabling sensitivity to the mid–lower troposphere to be minimised, providing complementary information to IASI.

Whilst these results for the LHR are promising, much of the impact of IASI results from the excellent global coverage the instrument provides due to its wide swath.

The actual impact of an LHR in NWP would rely on some method of establishing global coverage, possibly with a push-broom multi-instrument configuration, or a constellation. The study also identified that there was a high probability of information on water vapour content very high in the atmosphere, using the region of the spectrum between $500\text{ and }600\text{ cm}^{-1}$. This promising avenue should be pursued if the reliability of background covariance information can be improved.

This study concludes that a multiplexing LHR is worthy of consideration as an instrument for NWP on both LEO and GEO platforms. It is of particular interest for filling in the upper-atmosphere gap in the operational satellite observing system. Further research should be undertaken to develop multiplexing technology that would yield an instrument that could be used for mid-to-upper atmospheric sounding.

ACKNOWLEDGEMENTS

This work was carried out with financial support from The Science and Technology Facilities Council Global Challenge Concepts Scheme, award number ST/M007154/1.

ORCID

Fiona Smith  <http://orcid.org/0000-0002-8068-913X>

Stephan Havemann  <http://orcid.org/0000-0002-3259-091X>

Alex Hoffmann  <https://orcid.org/0000-0003-1247-8135>

Damien Weidmann  <https://orcid.org/0000-0002-0178-7904>

REFERENCES

- Allario, F., Katzberg, S.J. and Hoell, J.M. (1983) Tunable laser heterodyne spectrometer measurements of atmospheric species. In: Killinger, D.K. and Mooradian, A. (Eds.) *Optical and Laser Remote Sensing*. Berlin, Heidelberg: Springer, pp. 50–70. https://doi.org/10.1007/978-3-540-39552-2_8.
- Andersson, E., Fisher, M., Munro, R. and McNally, A. (2000) Diagnosis of background errors for radiances and other observable quantities in a variational data assimilation scheme, and the explanation of a case of poor convergence. *Quarterly Journal of the Royal Meteorological Society*, 126, 1455–1472.
- Clough, S., Shephard, M.W., Mlawer, E., Delamere, J.S., Iacono, M., Cady-Pereira, K., Boukabara, S. and Brown, P.D. (2005) Atmospheric radiative transfer modeling: a summary of the AER codes. *Journal of Quantitative Spectroscopy and Radiative Transfer*, 91, 233–244. <https://doi.org/10.1016/j.jqsrt.2004.05.058>.
- Collard, A., Hilton, F., Forsythe, M. and Candy, B. (2011) From observations to forecasts – Part 8: The use of satellite observations in numerical weather prediction. *Weather*, 66, 31–36. <https://doi.org/10.1002/wea.736>.
- Deeter, M.N., Edwards, D.P., Gille, J.C., Emmons, L.K., Francis, G., Ho, S.-P., Mao, D., Masters, D., Worden, H., Drummond, J.R. and Novelli, P.C. (2010) The MOPITT version 4 CO product: algorithm enhancements, validation, and long-term stability. *Journal of Geophysical Research*, 115, D07306. <https://doi.org/10.1029/2009JD013005>.
- Desroziers, G., Berre, L., Chapnik, B. and Poli, P. (2005) Diagnosis of observation, background and analysis error statistics in observation space. *Quarterly Journal of the Royal Meteorological Society*, 131, 3385–3396.
- Dudhia, A. (2016) The reference forward model (RFM). *Journal of Quantitative Spectroscopy and Radiative Transfer*, 186, 243–253. <https://doi.org/10.1016/j.jqsrt.2016.06.018>.

- Eyre, J.R. and Hilton, F.I. (2013) Sensitivity of analysis error to the mis-specification of background error covariance. *Quarterly Journal of the Royal Meteorological Society*, 139, 524–533. <https://doi.org/10.1002/qj.1979>.
- Grant, D., Dudek, R., Buchanan, M. and Liu, H.C. (2006) Room-temperature heterodyne detection up to 110 GHz with a quantum-well infrared photodetector. *IEEE Photonics Technology Letters*, 18(21), 2218–2220. <https://doi.org/10.1109/LPT.2006.884267>.
- Havemann, S. (2006) The development of a fast radiative transfer model based on an empirical orthogonal functions (EOF) technique. *SPIE Proceedings*, 6405, 4050–4058. <https://doi.org/10.1117/12.693995>.
- Havemann, S. (2015) *Report on global comparisons of HT-FRTC with traditional RTTOV calculations*. Met Office Internal Report.
- Havemann, S., Thelen, J.-C., Taylor, J.P. and Harlow, R.C. (2016) The Havemann–Taylor fast radiative transfer code (HT-FRTC): a multipurpose code based on principal components. *Journal of Quantitative Spectroscopy and Radiative Transfer*. <https://doi.org/10.1016/j.jqsrt.2018.09.008>.
- Hilton, F.I., Antonelli, P., Calbet, X., Hultberg, T., Lavanant, L., Liu, X., Masiello, G., Newman, S., Taylor, J., Serio, C. and Zhou, D. (2009a) An investigation into the performance of retrievals of temperature and humidity from IASI. *Proc 2009 Eumetsat Meteorological Satellite Conference*, 21–25 September 2009, Bath, UK. Available at: http://www.eumetsat.int/website/wcm/idc/idcplg?IdcService=GET_FILE&dDocName=PDF_CONF_P55_S7_37_HILTON_P&RevisionSelectionMethod=LatestReleased&Rendition=Web [Accessed 29 August 2018].
- Hilton, F.I., Atkinson, N., English, S. and Eyre, J.R. (2009b) Assimilation of IASI at the Met Office and assessment of its impact through observing system experiments. *Quarterly Journal of the Royal Meteorological Society*, 135(639), 495–505. <https://doi.org/10.1002/qj.379>.
- Hilton, F.I., Armante, R., August, T., Barnet, C., Bouchard, A., Camy-Peyret, C., Capelle, V., Clarisse, L., Clerbaux, C., Coheur, P., Collard, A., Crevoisier, C., Dufour, G., Edwards, D., Fajjan, F., Fourrié, N., Gambacorta, A., Goldberg, M., Guidard, V., Hurtmans, D., Illingworth, S., Jacquinet-Husson, N., Kerzenmacher, T., Klaes, D., Lavanant, L., Masiello, G., Matricardi, M., McNally, A., Newman, S., Pavelin, E., Payan, S., Péquignot, E., Peyridieu, S., Phulpin, T., Remedios, J., Schlüssel, P., Serio, C., Strow, L., Stubenrauch, C., Taylor, J., Tobin, D., Wolf, W. and Zhou, D. (2012) Hyperspectral Earth observation from IASI: five years of accomplishments. *Bulletin of the American Meteorological Society*, 93, 347–370. <https://doi.org/10.1175/BAMS-D-11-00027.1>.
- Hoffmann, A., Macleod, N.A., Huebner, M. and Weidmann, D. (2016) Thermal infrared laser heterodyne spectroradiometry for solar occultation atmospheric CO₂ measurements. *Atmospheric Measurement Techniques*, 9, 5975–5996. <https://doi.org/10.5194/amt-9-5975-2016>.
- Janjić, T., Bormann, N., Bocquet, M., Carton, J.A., Cohn, S.E., Dance, S.L., Losa, S.N., Nichols, N.K., Potthast, R., Waller, J.A. and Weston, P. (2017) On the representation error in data assimilation. *Quarterly Journal of the Royal Meteorological Society*. <https://doi.org/10.1002/qj.3130>.
- Lorenc, A.C. and Marriott, R.T. (2014) Forecast sensitivity to observations in the Met Office Global numerical weather prediction system. *Quarterly Journal of the Royal Meteorological Society*, 140, 209–224. <https://doi.org/10.1002/qj.2122>.
- Mumma, M.J., Kostiuk, T., Duhl, D., Chin, G. and Zipoy, D. (1982) Infrared heterodyne spectroscopy. *Optical Engineering*, 21(2), 212–313. <https://doi.org/10.1117/12.7972901>.
- Myers, T.L., Cannon, B.D., Brauer, C.S., Hansen, S.M. and Crowther, B.G. (2015) Proton and gamma irradiation of Fabry–Perot quantum cascade lasers for space qualification. *Applied Optics*, 54, 527–534.
- Rawlins, F., Ballard, S.P., Bovis, K.J., Clayton, A.M., Li, D., Inverarity, G.W., Lorenc, A.C. and Payne, T.J. (2007) The Met Office global four-dimensional variational data assimilation scheme. *Quarterly Journal of the Royal Meteorological Society*, 133, 347–362. <https://doi.org/10.1002/qj.32>.
- Rodgers, C.D. (2000) *Inverse Methods for Atmospheric Sounding: Theory and Practice*. Singapore: World Scientific.
- Rothman, L.S., Gordon, I.E., Babikov, Y., Barbe, A., Benner, D.C., Bernath, P.F., Birk, M., Bizzocchi, L., Boudon, V., Brown, L.R. and Campargue, A. (2013) The HITRAN2012 molecular spectroscopic database. *Journal of Quantitative Spectroscopy and Radiative Transfer*, 130, 4–50. <https://doi.org/10.1016/j.jqsrt.2013.07.002>.
- Schieder, R., Tolls, V. and Winnewisser, G. (1989) The Cologne acousto-optical spectrometers. *Experimental Astronomy*, 1, 101–121.
- Siegman, A.E. (1966) The antenna properties of optical heterodyne receivers. *Proceedings of the IEEE*, 54(10), 1350–1356. <https://doi.org/10.1109/PROC.1966.5122>.
- Siméoni, D., Singer, C. and Chalon, G. (1997) Infrared atmospheric sounding interferometer. *Acta Astronautica*, 40, 113–118.
- Smith, F.I. (2015) *Improving the information content of IASI assimilation for numerical weather prediction*. PhD thesis, Leicester, UK: University of Leicester. Available at: <https://ira.le.ac.uk/handle/2381/32040> [Accessed 28 August 2018].
- Tsai, T.R., Rose, R.A., Weidmann, D. and Wysocki, G. (2012) Atmospheric vertical profiles of O₃, N₂O, CH₄, CCl₂F₂, and H₂O retrieved from external-cavity quantum-cascade laser heterodyne radiometer measurements. *Applied Optics*, 51, 8779–8792. <https://doi.org/10.1364/AO.51.008779>.
- Wang, L., Chen, Y. and Han, Y. (2016) Impacts of field of view configuration of cross-track infrared sounder on clear sky observations. *Applied Optics*, 55(25), 7113–7119.
- Weidmann, D., Reburn, W.J. and Smith, K.M. (2007a) Ground-based prototype quantum cascade laser heterodyne radiometer for atmospheric studies. *Review of Scientific Instruments*, 78(7), 073107. <https://doi.org/10.1063/1.2753141>.
- Weidmann, D., Reburn, W.J. and Smith, K.M. (2007b) Retrieval of atmospheric ozone profiles from an infrared quantum cascade laser heterodyne radiometer: results and analysis. *Applied Optics*, 46, 7162–7171. <https://doi.org/10.1364/AO.46.007162>.
- Weidmann, D., Tsai, T., Macleod, N.A. and Wysocki, G. (2011a) Atmospheric observations of multiple molecular species using ultra-high-resolution external cavity quantum cascade laser heterodyne radiometry. *Optics Letters*, 36, 1951–1953. <https://doi.org/10.1364/OL.36.001951>.
- Weidmann, D., Perrett, B.J., Macleod, N.A. and Jenkins, R.M. (2011b) Hollow waveguide photomixing for quantum cascade laser heterodyne spectro-radiometry. *Optics Express*, 19, 9074–9085. <https://doi.org/10.1364/OE.19.009074>.
- Weidmann, D., Hoffmann, A., Macleod, N., Middleton, K., Kurtz, J., Barraclough, S. and Griffin, D. (2017) The Methane Isotopologues by Solar Occultation (MISO) nanosatellite mission: spectral channel optimization and early performance analysis. *Remote Sensing*, 9, 1073. <https://doi.org/10.3390/rs9101073>.
- Weston, P.P., Bell, W. and Eyre, J.R. (2014) Accounting for correlated error in the assimilation of high resolution sounders. *Quarterly Journal of the Royal Meteorological Society*, 140, 2420–2429. <https://doi.org/10.1002/qj.2306>.
- Wlasak, M.A. (2013) *VAR technical documentation paper 46_1: randomisation method for background covariance estimates*. Internal Met Office Documentation Paper VTDP 46_1.
- Wlasak, M.A. and Cullen, M.J.P. (2014) Modelling static 3-D spatial background error covariances – the effect of vertical and horizontal transform order. *Advances in Science and Research*, 11, 63–67. <https://doi.org/10.5194/asr-11-63-2014>.

How to cite this article: Smith F, Havemann S, Hoffmann A, Bell W, Weidmann D, Newman S. Evaluation of laser heterodyne radiometry for numerical weather prediction applications. *Q J R Meteorol Soc* 2018;1–20. <https://doi.org/10.1002/qj.3365>